TECHNISCHE UNIVERSITÄT WIEN

ATOMINSTITUT

DIPLOMARBEIT

Thermodynamics of the extended Dicke model

zur Erlangung des akademischen Grades

Diplom-Ingenieur

im Rahmen des Studiums

Technische Physik

ausgeführt am Atominstitut der Fakultät für Physik
der Technischen Universität Wien
unter der Anleitung von

Associate Prof. Dr. Peter Rabl

durch

Philipp Pilar
Matrikelnummer 01226110

Datum	Verfasser	Betreuer

Abstract

The derivation of effective light-matter Hamiltonians in the context of cavity QED is revisited and the importance of making the correct choice of gauge is demonstrated. Controversies surrounding the quantum Rabi model as to whether the ultrastrong coupling regime can be reached are resolved and the adequacy of the effective models when applied to a superconducting circuit setup is shown. The effects of finite temperatures on the superradiant phase transition and the crossover to the subradiant phase in the extended Dicke model are exhibited. Applicability and limitations of the Holstein-Primakoff approximation as well as a mean field approach to the extended Dicke model are investigated. The heat capacity of the extended Dicke model is examined for a broad range of parameters.

Acknowledgements

First of all, I would like to thank my supervisor Peter Rabl who has always been supportive of me. Whenever I was confused he patiently answered my questions and guided my efforts in the right direction. Thank you, Peter, for introducing me to the world of conducting research!

My special thanks also go to Daniele De Bernardis, with whom I collaborated extensively over the past year. It has been a pleasure working with you, Daniele!

Furthermore, I would like to thank the remaining members of the 'rablgroup'. Everybody was friendly and accommodating and made the time spent there enjoyable. Thank you, Tuomas, Julian, Giuseppe, Yuri and Peter!

Finally, I want to thank my family and friends. They have always supported me in my endeavours but at the same time they reminded me that there is more to life than physics.

Contents

Overview

The extended Dicke model (EDM) [1, 2] is a quantum-optical model that describes the interaction between N two-level atoms, or qubits, and one bosonic field mode. As the name suggests, it is a generalized version of the Dicke model [3, 4] that includes additional qubit-qubit interactions. These interactions can give rise to very different system properties, as is exemplified by the prediction of a superradiant phase transition (SRT) [5, 6, 7] for ferromagnetic interactions and that of a crossover to a subradiant phase [8] otherwise.

Many different physical platforms exist that can be accurately described by the EDM, e.g., atoms in a cavity [9, 10], superconducting circuits [11, 12, 13] or quantum dots [14, 15] to name just a few. Experimental methods are improving quickly, allowing for the implementation of stronger couplings between qubits and photons. In many of these settings, it has recently become possible to enter the so-called ultrastrong coupling regime [16, 17], where this coupling becomes the dominant energy scale of the system. In this regime the EDM predicts exciting new phenomenology, e.g., the aforementioned superradiant phase transition. There are, however, some controversies as to whether actual physical systems will yield parameters allowing for such a phase transition. In particular, so-called 'no-go theorems' have been discussed in the literature, claiming that it is impossible to reach this phase transition point, while in other works it is argued that such theorems do not hold [18, 19, 20].

The first part of this master thesis revisits the derivation of effective cavity QED models, starting from dipole-field interaction Hamiltonian expressed in different gauges. This analysis clearly shows that in the ultrastrong coupling regime, the validity of the usual two-level approximation depends crucially on the choice of gauge. This finding applies to both real dipoles as well as superconducting circuits and resolves the aforementioned controversies in both settings.

Having verified the validity of the extended Dicke model as an accurate description of

cavity QED systems in the ultrastrong coupling regime, the second part of this thesis then discusses the thermal equilibrium states of this model. Here I have used two approximations to gain some analytic results and to determine their range of validity: firstly, the Holstein-Primakoff approximation is employed to derive exactly solvable bilinear bosonic Hamiltonians and derive an expression for the electromagnetic energy of the system. Secondly, I use a mean field approach and compare the results. Furthermore, I calculate the specific heat of the EDM and investigate how the coupling between cavity and qubits impacts this quantity.

Finally, in the third part of the thesis, I briefly review the methods I used in the numerical simulations. Some analytic transformations which allow for more efficient numerical implementations of the EDM are presented. Furthermore, I explain how one can accurately estimate cutoffs for the photon number or the number of states to be taken into account.

Part I

Breakdown of gauge invariance in ultrastrong-coupling cavity QED

Introduction

In this part of the work we investigate the derivation of effective cavity-QED Hamiltonians and we point out the importance of making the correct choice of gauge when performing a 2-level approximation. In particular, we consider the derivation of the quantum Rabi model (QRM) [21] and the (extended) Dicke model (DM) [3, 4, 1], both of which are widely used as approximate descriptions of various quantum mechanical systems, like atoms in a cavity, certain superconducting circuits, or any other system which can effectively be described as a set of qubits interacting with a single oscillator. In spite of their common usage, controversies still surround these models in form of a 'no-go theorem' [18] and a 'counter no-go theorem' [19], claiming that the so-called (collective) ultrastrong coupling (USC) regime either cannot be reached or can be reached, respectively. USC occurs when the coupling strength between dipoles and oscillator becomes the dominating energy scale of the system, making it energetically favorable for excitations of the atomic system to be present in the ground state; in the many-dipole case, USC is a prerequisite for a superradiant phase transition to take place. We will show that a careful choice of gauge in the derivation of these models can resolve the aforementioned contradictory claims. Here it is important to properly take into account properties of the atomic potential, the most important qualitative factor being its anharmonicity. Finally, we are going to investigate the applicability of the correct effective model to a realistic physical setup in form of a superconducting circuit with flux-qubits.

The results discussed in this part of the work have been obtained in collaboration with Daniele de Bernardis in the group of Peter Rabl and have been published in Physical Review A [20]. For this publication I contributed most of the numerical calculations and the analysis of the circuit QED implementations.

Chapter 1

Breakdown of gauge invariance in ultrastrong-coupling cavity QED

1.1 The QRM in the Coulomb gauge

We begin our investigations with a very simple cavity-QED setup (see Fig. 1.1): a single-mode cavity containing one dipole. The dipole can be thought of as being an approximate description of an atom in the cavity. The dipole is described as an effective particle of mass m moving in a potential $V(x)$, where x is the separation of the two dipole charges.

Following the usual QED-procedure of minimal coupling, the Hamiltonian of this system can be written as

$$\begin{aligned} H_C &= \frac{(p-qA)^2}{2m} + V(x) + \hbar\omega_c a^\dagger a = \frac{p^2}{2m} + V(x) - \frac{qpA}{m} + \frac{q^2A^2}{2m} + \hbar\omega_c a^\dagger a \\ &= H_d(x) + H_{\text{int}}(x) + H_c, \end{aligned} \tag{1.1}$$

where $A = \mathcal{A}_0(a + a^\dagger)$ is the electromagnetic vector potential. As implied in the above formula this Hamiltonian essentially consists of 3 different contributions: $H_d(x) = \frac{p^2}{2m} + V(x)$ describes the internal dynamics of the dipole whereas $H_c = \hbar\omega_c a^\dagger a + \frac{q^2}{2m}A^2$ corresponds to the cavity mode and $H_{\text{int}}(x) = -\frac{qpA}{m}$ to the interaction between cavity and dipole.

We can simplify H_c by performing a Bogoliubov transformation (note that H_c is a special case of a bilinear bosonic Hamiltonian; general methods on how to diagonalize such Hamiltonians are discussed in section 4.2) on the bosonic operators: we define new creation

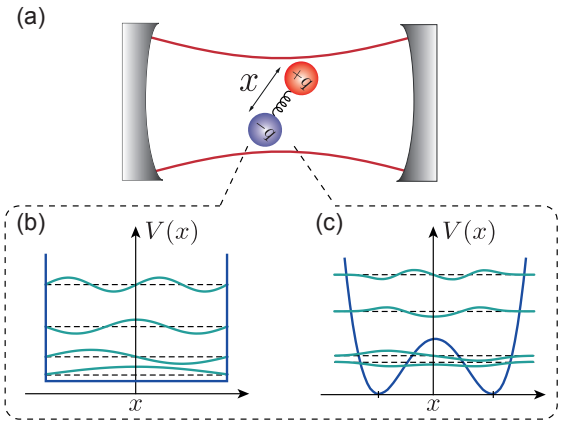

Figure 1.1: *(a) The cavity-QED setup under consideration: a single-mode cavity containing a dipole consisting of two electric charges, +q and -q, seperated by a distance x. The dipole can be interpreted as a simplified representation of an underlying atomic system. Using the dipole separation x as a spatial coordinate we can model the dipole as an effective particle moving in a potential V(x), since the potential energy depends on the charge separation. In our analysis we are going to focus on the two potentials depicted in the figure: (b) a slightly anharmonic square-well potential and (c) a double-well potential with very high anharmonicity.*

and annihilation operators c, $c^\dagger$ via

$$c = \mu a - \nu a^\dagger, \tag{1.2}$$

$$c^\dagger = \mu^\star a^\dagger - \nu^\star a. \tag{1.3}$$

The parameters μ and ν must be chosen in a way such as to reproduce the cavity Hamiltonian

$$H_c = \left(\hbar\omega_c + 2\frac{q^2}{2m}\right) a^\dagger a + \frac{q^2}{2m}\left(a^2 + a^{\dagger 2} + 1\right) \stackrel{!}{=} \hbar\tilde{\omega}_c c^\dagger c + C \tag{1.4}$$

and such that the new operators c, $c^\dagger$ fulfill the bosonic commutation relations

$$[c, c^\dagger] = 1. \tag{1.5}$$

Relation (1.5) yields the requirement $|\mu|^2 - |\nu|^2 = 1$ which suggests the ansatz

$$\mu = e^{i\theta_1}\cosh(r), \tag{1.6}$$

$$\nu = e^{i\theta_2}\sinh(r). \tag{1.7}$$

Plugging

$$c^\dagger c = |\mu|^2 a^\dagger a + |\nu|^2 a a^\dagger - \nu^\star \mu a^2 - \mu^\star \nu a^{\dagger 2} \tag{1.8}$$

into equation (1.4), choosing $\theta_1 = 0$, $\theta_2 = \pi$ and comparing coefficients on both sides yields the required parameters

$$\tilde{\omega}_c = \sqrt{\omega_c^2 + 2\omega_c \frac{q^2 A_0^2}{\hbar m}} := \sqrt{\omega_c^2 + D^2}, \tag{1.9}$$

$$r = \frac{1}{2}\operatorname{arcosh}\left(\frac{\hbar\omega_c + \frac{q^2\mathcal{A}_0^2}{m}}{\hbar\tilde{\omega}_c}\right), \tag{1.10}$$

$$\mu = \sqrt{\frac{\omega_c + \frac{q^2 A_0^2}{m} + \tilde{\omega}_c}{2\tilde{\omega}_c}}, \tag{1.11}$$

$$\nu = \sqrt{\frac{\omega_c + \frac{q^2 A_0^2}{m} - \tilde{\omega}_c}{2\tilde{\omega}_c}}, \tag{1.12}$$

$$C = -\frac{\hbar\omega_c - \hbar\tilde{\omega}_c}{2}. \tag{1.13}$$

Using the relation

$$a + a^\dagger = (\mu + \nu)(c + c^\dagger) = \sqrt{\frac{\omega_c}{\tilde{\omega}_c}}(c + c^\dagger), \tag{1.14}$$

which follows from (1.2), the interaction part of the Hamiltonian can also be expressed in terms of c, $c^\dagger$ as

$$H_{\text{int}} = -\frac{qp\mathcal{A}_0}{m}\sqrt{\frac{\omega_c}{\tilde{\omega}_c}}(c + c^\dagger). \tag{1.15}$$

The entire Hamiltonian then reads

$$H_C = \hbar\tilde{\omega}_c c^\dagger c + \frac{p^2}{2m} + V(x) - \frac{qp\mathcal{A}_0}{m}\sqrt{\frac{\omega_c}{\tilde{\omega}_c}}(c + c^\dagger) - \frac{\hbar\omega_c - \hbar\tilde{\omega}_c}{2}. \tag{1.16}$$

In the following, when demonstrating the results of our analysis by means of concrete atomic potentials, we are going to consider two different cases: a square-well potential of

rather low anharmonicity and a highly anharmonic double-well potential. Here we have defined the anharmonicity, or non-linearity, of a potential as the ratio

$$\Delta_{nl} = \frac{\omega_2 - \omega_0}{\omega_1 - \omega_0} = \frac{\omega_{20}}{\omega_{10}}, \tag{1.17}$$

where $\hbar\omega_n$ is the energy of the n-th energy level. High anharmonicity as per our definition is therefore equivalent to the existence of an energetically well isolated qubit-subspace, consisting of ground state and first excited state of the atomic system.

As mentioned in the introduction we want to derive approximate light-matter Hamiltonians in different gauges and investigate the validity of the resulting models. The minimal coupling Hamiltonian (1.1), which we have written down at the beginning of this section, is in the so-called Coulomb gauge. The next step on our way to an effective Hamiltonian is to perform a two-level approximation (TLA). At this point we would expect the approximation to yield reasonable results for potentials with high anharmonicity due to energetic suppression of higher lying states. The procedure of performing a TLA goes as follows: calculate both eigenspectrum and eigenstates of the dipole Hamiltonian $H_d(x)$, write operators acting non-trivially in the dipole-space in the dipole eigenbasis via $O = \sum_{ij} O_{ij} \left|\phi_i\right\rangle \left\langle\phi_j\right|$ where $O_{ij} = \langle\phi_i|O|\phi_j\rangle$ and then truncate the Hilbert space such that only the ground state and the first excited state remain. We can then write H_C as

$$H_C = \frac{\hbar\omega_{01}}{2}\sigma_z - \frac{\hbar g_C}{2}\sigma_y(c + c^\dagger) + \hbar\tilde{\omega}c^\dagger c - \frac{\hbar\omega_c - \hbar\tilde{\omega}_c}{2} \tag{1.18}$$

$$= \hbar\omega_{01}\sigma_z + \hbar g_C\sigma_x(c + c^\dagger) + \hbar\tilde{\omega}c^\dagger c - \frac{\hbar\omega_c - \hbar\tilde{\omega}_c}{2}, \tag{1.19}$$

where the σ_i are Pauli matrices and $g_C = \frac{2qA_0|p_{01}|}{\hbar m}\sqrt{\frac{\omega_c}{\tilde{\omega}_c}} = \sqrt{\frac{2}{\hbar m\tilde{\omega}_c}}D|p_{01}|$; in the last step we have performed a rotation in spin space to receive the quantum Rabi model in its common form. In the next section we are going to investigate whether the parameters derived in this section allow for the QRM to enter the ultrastrong coupling regime.

1.1.1 No-go theorem

While in order for a superradiant phase transition to take place multiple dipoles would be required, a qualitative change of the ground state can also be observed in the QRM [22], when the dimensionless coupling parameter ζ_C takes on values larger than one, i.e. when $\zeta_C = \frac{g_C^2}{\tilde{\omega}_c\omega_{10}} > 1$. As the coupling strength approaches g_c an exponential decrease of the

energy gap between ground state and first excited state sets in, leading to a near-degenerate ground-state manifold.

To check whether this condition can be fulfilled in case of the Coulomb gauge QRM we are going to derive a bound for ζ_C. To this end we will need the Thomas-Reiche-Kuhn (TRK) sum rule, which can be derived as follows: consider the commutator $[x,[x,H(x)]]$, where $H(x)$ is is a Hamiltonian of the general form $H(x) = \frac{p^2}{2m} + V(x)$. Making use of $[x,p] = i\hbar$ and hence $[x,H(x)] = \frac{i\hbar p}{m}$ allows us to write the commutator as

$$[x,[x,H]] = x(xH - Hx) - (xH - Hx)x = \left[x, \frac{i\hbar p}{m}\right] = -\frac{\hbar^2}{m}. \tag{1.20}$$

Calculating the ground state expectation value of this expression delivers

$$\langle\phi_0|[x,[x,H]]|\phi_0\rangle = 2\sum_n (\langle\phi_0|x|\phi_n\rangle \langle\phi_n|x|\phi_0\rangle \hbar\omega_0 - \langle\phi_0|x|\phi_n\rangle \langle\phi_n|x|\phi_0\rangle \hbar\omega_n) \tag{1.21}$$

$$= 2\sum_n \hbar(\omega_0 - \omega_n)|\langle\phi_n|x|\phi_0\rangle|^2 = -\frac{\hbar^2}{m}. \tag{1.22}$$

Equation (1.22) is called the TRK sum rule. Using $\omega_n > \omega_0$ and $|\langle\phi_n|x|\phi_0\rangle|^2 > 0$ we can derive the following inequality for the absolute value of the x_{01} matrix element:

$$|x_{01}|^2 < \frac{\hbar}{2m\omega_{10}}. \tag{1.23}$$

Using the relation $p_{ij} = imx_{ij}(\omega_j - \omega_i)$ between position and momentum matrix elements we see that the bound for the x matrix element also implies a bound for the p matrix element. Using this bound we can show that

$$\zeta_C = \frac{g_C^2}{\tilde{\omega}_c\omega_{10}} = \frac{2\omega_c|p_{01}|^2D^2}{\hbar m\tilde{\omega}_c^2\omega_{10}} = \frac{D^2}{\omega_c^2 + D^2} f \leq 1, \tag{1.24}$$

where $f = \frac{2m\omega_{10}|x_{01}|^2}{\hbar}$ is the so-called oscillator strength. In general, the oscillator strength characterizes how strongly a transition between two states of a quantum system couples to the electromagnetic field. The TRK sum rule can be used to show that $f \leq 1$ and since $\frac{D^2}{\omega_c^2+D^2} < 1$ inequality (1.24) immediately follows. When dealing with artificial atoms it is important to keep in mind that a commutation relation of the form $[x,p] = i\hbar$ is required for this argument to work.

Thus we have shown that a transition to the USC regime cannot take place in the Coulomb gauge QRM. Essentially, the renormalization of the cavity frequency due to the A^2-term suppresses the transition. This result is known as the no-go theorem.

1.2 The QRM in the electric dipole gauge

Let us now re-derive the QRM in a different gauge, the so-called electric dipole gauge. Using the unitary transformation $T = e^{-\frac{i}{\hbar}xA_0(a^\dagger+a)}$ under which $p \to p + qA$ and $a^\dagger a \to a^\dagger a + ix'(a^\dagger - a) + x'^2$, where $x' = \frac{qA_0}{\hbar}x$, we can transform the minimal-coupling Hamiltonian via $H_D = TH_CT^\dagger$ and receive the corresponding Hamiltonian in the dipole gauge:

$$H_D = \frac{p^2}{2m} + V(x) + \hbar\omega_c x'^2 + i\hbar\omega_c x'(a^\dagger - a) + \hbar\omega_c a^\dagger a. \tag{1.25}$$

Essentially, the gauge transformation has effected two changes: the A^2-term has been exchanged for an x^2-term and the coupling between cavity and dipole is now mediated by the position instead of the momentum operator. The x^2-term can be treated in two ways: either, we can add it to the potential to get $\tilde{V}(x) = V(x) + \hbar\omega x'^2$ or we can leave it outside (after the TLA this term would be $\propto \sigma_x^2$ and therefore constant). In the following we are going to include it in the potential since, intuitively, on might expect that this will lead to more accurate results than effectively neglecting it. The modified potential results in different eigenstates and eigenvalues which we will denote as $|\tilde{\varphi}\rangle$. Following the same procedure as previously in the Coulomb picture we can again perform a 2-state approximation and arrive at

$$H_D = \hbar\frac{\tilde{\omega}_{01}}{2}\sigma_z + i\hbar\frac{g_D}{2}\sigma_x(a^\dagger - a) + \hbar\omega_c a^\dagger a \tag{1.26}$$

$$= \hbar\frac{\tilde{\omega}_{01}}{2}\sigma_z + \hbar\frac{g_D}{2}\sigma_x(a^\dagger + a) + \hbar\omega_c a^\dagger a \tag{1.27}$$

with $g_D = \frac{2\omega q\mathcal{A}_0|\tilde{x}_{01}|}{\hbar}$; in the last step we have rotated our photon operators as $a \to ia$. Hence we receive again the QRM Hamiltonian, albeit with different parameters. In the next section we are going to find out whether these different parameters also lead to qualitatively different predictions.

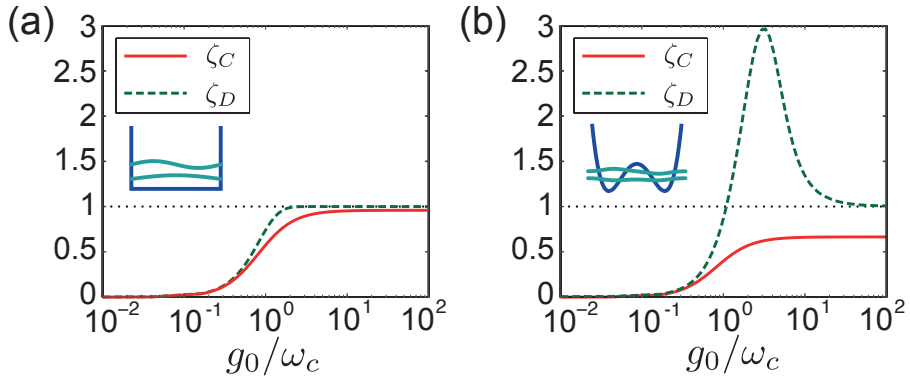

Figure 1.2: *The dimensionless coupling parameters ζ_C and ζ_D of the Coulomb and the dipole picture respectively are plotted as a function of the coupling strength g_0, as defined in equation (1.29). In case of (a) a square well potential and (b) a double well potential with $\beta = 2.4$ have been assumed. See the definition in Hamiltonian (1.30). While ζ_C remains below one for both potentials, consistent with the no-go theorem, ζ_D can exceed this threshold in case of the double-well potential, hence the quantum Rabi model enters the USC.*

1.2.1 Counter no-go theorem

Analogous to the derivation of the bound for the dimensionless coupling parameter in the Coulomb picture we can also derive a bound in the dipole picture and find

$$\zeta_D = \frac{g_D^2}{\omega_c \tilde{\omega}_{01}} = \frac{4\omega q A_0 |\tilde{x}_{01}|}{\hbar \tilde{\omega}_{01}} = \frac{D^2}{\tilde{\omega}_{01}^2} \tilde{f} \leq \frac{D^2}{\tilde{\omega}_{01}^2}. \tag{1.28}$$

Like before, we have used the TRK sum rule to show that the oscillator strength $\tilde{f} = \frac{2m\tilde{\omega}_{01}|\tilde{x}_{10}|^2}{\hbar} \leq 1$. This time, however, there is no general constraint for the first factor $\frac{D^2}{\tilde{\omega}_{01}^2}$ and the USC regime can in principle be reached. The quantities $\tilde{\omega}_{01}$ and D required to determine its existence can be derived from the modified atomic potential $\tilde{V}(x)$ and by taking into account the remaining parameters of the QRM.

1.3 Validity of the two-level approximation

Having derived contradictory results for the two different gauges in the previous sections we would now like to investigate in which gauge the QRM makes accurate predictions and up to what coupling strengths the two-state approximation holds. To this end we simulate the QRM for the case of a resonant oscillator and qubit, i.e. where $\omega_c = \omega_{10}$, and compare

the results to those received by simulating the full minimal coupling Hamiltonian (where we take into account all dipole states). As mentioned previously, we are going to do this for two different dipole potentials, the only slightly anharmonic infinite square-well potential and a highly anharmonic double-well potential. We will plot our findings against the coupling strength

$$\frac{g_0}{\omega_c} = \frac{g_D}{\omega_c}\frac{x_{01}}{\tilde{x}_{01}}, \tag{1.29}$$

which basically is the coupling strength in the dipole picture but with the influence of the x^2-term on the x_{01} matrix-element factored out.

Concerning the possibility or impossibility of USC, we now take a look at Fig. 1.2 where ζ_C and ζ_D are plotted for both potentials. As predicted, in the Coulomb-picture a transition to the USC regime occurs for neither of the potentials, in the dipole gauge, however, the coupling parameter crosses the threshold of one indicating the occurence of USC over a certain range of coupling-strengths. It remains to be shown which of the two is correct.

1.3.1 Double-well potential

Our double-well potential is of the form

$$V(x) = -\frac{\mu}{2}x^2 + \frac{\lambda}{4}x^4 = E_d\left(-\frac{\beta}{2}\xi^2 + \frac{\xi^4}{4}\right), \tag{1.30}$$

where $E_d = \hbar^2/(mx_0^2)$, $\xi = x/x_0$, $x_0 = \sqrt[6]{\hbar^2/(m\lambda)}$ and $\beta = \mu x_0^2/E_d$. Now, the shape of the double well can be controlled by tuning β; a value of $\beta = 0$ would mean a quartic potential, increasing it leads to a double well with increasing depth and hence increasing non-linearity.

In Fig. 1.3 results for a double-well with $\beta = 3.8$ are plotted. For this value of β the potential has a very high non-linearity of $\Delta_{nl} > 100$. In subfigure 1.3 (a) the spectrum of the full model as well as those of the corresponding QRM Hamiltonians in the Coulomb and dipole picture are depicted. Whereas the dipole-QRM shows excellent agreement with the exact model, even deep into the ultrastrong coupling regime, the approximation in the Coulomb picture breaks down rather early at coupling strengths $g_0 \gtrsim 0.1$. Subfigures (b) and (c) clarify the origins of this discrepancy. In these plots the magnitude of the matrix elements of both the position and momentum operator are depicted. The position operator exhibits a well isolated qubit-subspace with only weak couplings to higher lying states. For

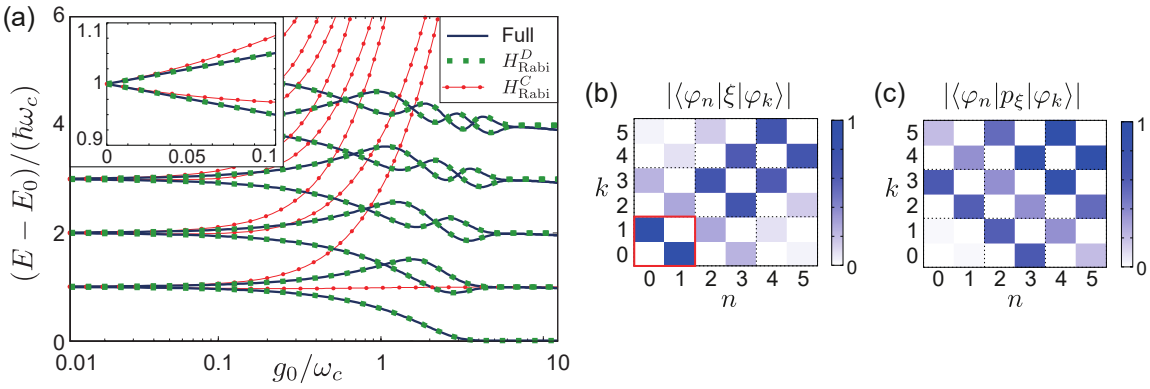

Figure 1.3: *Double-well potential ($\beta = 3.8$): (a) The spectrum of the full minimal coupling Hamiltonian (solid blue line) and the spectra of the approximate two-state quantum Rabi Hamiltonians in the Coulomb gauge (red dotted line) and in the dipole gauge (green dashed line) are depicted for coupling strengths up to the USC, as well as a close-up of the weak coupling regime. It is immediately obvious that the approximation in the Coulomb picture is totally wrong for coupling strengths $g \gtrsim 0.1$. The QRM in the dipole picture, on the other hand, shows excellent agreement up to coupling strengths deep in the ultrastrong coupling regime. (b) Matrix elements of the position operator: the qubit-subspace is well isolated from the remaining Hilbert space in terms of matrix transition elements; apart from the high anharmonicity of the potential this is the main reason for the validity of the 2-state approximation in the dipole gauge. (c) Matrix elements of the momentum operator: the qubit subspace is not well isolated, on the contrary, coupling to higher states is stronger than the coupling between the qubit-states. Hence transitions to higher states will often occur, invalidating the 2-state approximation. Values of the matrix elements have been normalized to the largest one still visible in each plot.*

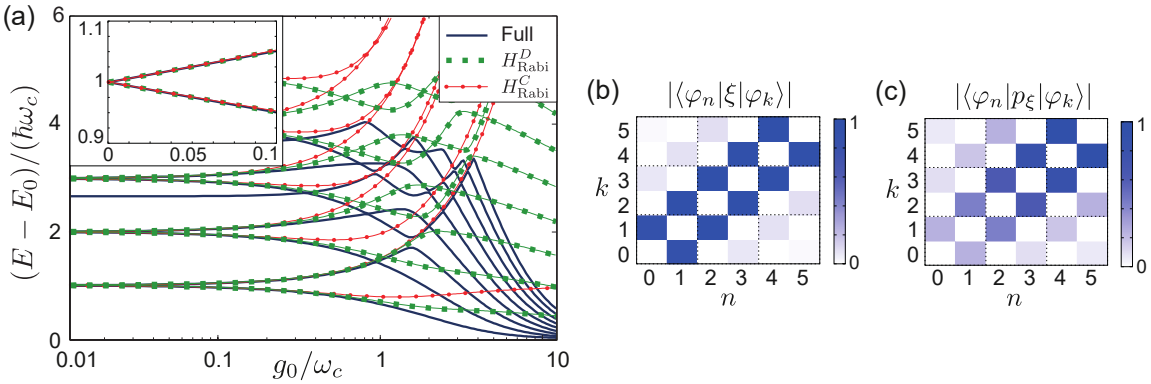

Figure 1.4: *Square-well potential: (a) The spectrum of the full minimal coupling Hamiltonian (solid blue line) and the spectra of the approximate two-state quantum Rabi Hamiltonians in the Coulomb gauge (red dotted line) and in the dipole gauge (green dashed line) are depicted for coupling strengths up to the USC, as well as a close-up of the weak coupling regime. While the dipole-QRM still produces better results, the 2-state approximation breaks down in the USC (or earlier in case of the Coulomb picture) in both Coulomb and dipole gauge. Note that for this less non-linear potential the Coulomb-gauge actually works better for weak coupling strengths than before in case of the double-well. (b) Matrix elements of the position operator: the qubit-subspace is less isolated than before, this fact together with a low non-linearity leads to the early breakdown of the 2-state approximation at values of* $\frac{g_0}{\omega_c} \sim 1$ *in case of the dipole picture. (c) Matrix elements of the momentum operator: the qubit-subspace is still not isolated. Matrix-elements of both position- and momentum-operator now resemble those of the harmonic oscillator. Values of the matrix elements have been normalized to the largest one still visible in each plot.*

the momentum operator, however, there exists no such subspace, in fact the qubit states are coupled more strongly to higher lying states than to each other. As the spectrum demonstrates, even in case of a highly non-linear potential the energy gap does not suffice to confine excitations to the qubit-subspace.

These results clearly demonstrate that the dipole gauge is the correct gauge to perform the two-level approximation in.

1.3.2 Square-well potential

Next, we would like to investigate an infinite square well potential which corresponds to a potential $V(x) = 0$ for $|x| < L/2$ and $V(x) = \infty$ everywhere else. The energy levels of the infinite box are given by $E_n = \frac{n^2\pi^2\hbar^2}{2mL^2}$ and we find a non-linearity of $\Delta_{nl} = \frac{8}{3}$, irrespective of

the width, which is considerably less than in the previous case of the double-well potential. Fig. 1.4 depicts the resulting energy spectra: in subfigure (a) the spectrum is depicted and this time, while the dipole gauge is still the better choice with good agreement up to $\frac{g_0}{\omega_c} \approx 0.3$, the differences between Coulomb and dipole picture in the 2-state approximation are far less pronounced. Interestingly, for small coupling strengths, the Coulomb gauge QRM actually delivers better results than previously for the more non-linear potential. Subfigures (b) and (c) show again the matrix elements of position and momentum operator. Note, that the qubit-subspace in the dipole picture is now significantly less isolated than before; in fact, the matrix elements now closely resemble those of the harmonic oscillator. This different structure of the Hilbert space aswell as the small energy gap are the main reason why the two-state approximation in the dipole-QRM doesn't work so well anymore in case of the square-well potential.

1.4 Many-dipole cavity QED

Having so far considered a setup with only one dipole we are now going to extend our discussion to the many-dipole case, i.e. the limit $N \to \infty$, $q \to 0$, $N\sqrt{q} = const$, where we have N dipoles in a cavity. In this limit the derivation of analytic results is possible which, while interesting in their own right, are useful as a crosscheck for simulations of systems with large but finite N.

We start again with the minimal coupling Hamiltonian in the Coulomb gauge

$$H_C = \sum_{i=1}^{N} \left[\frac{(p_i - qA)^2}{2m} + V(x_i) \right] + \hbar\omega_c a^\dagger a, \tag{1.31}$$

or, utilizing the gauge transformation $U = \exp\left(-i\frac{qA}{\hbar}\sum_i x_i(a + a^\dagger)\right)$, the equivalent Hamiltonian in the dipole gauge

$$H_D = \sum_i \left[\frac{p_i^2}{2m} + \tilde{V}(x_i) \right] + \frac{mD^2}{2} \sum_{i \neq j} x_i x_j + \hbar\omega_c a^\dagger a + i\omega_c q\mathcal{A}_0(a^\dagger - a) \sum_i x_i. \tag{1.32}$$

The most notable difference to the single-dipole case is the additional all-to-all coupling term that is now present in the dipole gauge. Note however, that this term does not correspond to any actual direct interactions between the dipoles, which we have not taken into account in our derivation, but is merely a result of the choice of gauge. Taking the

same steps as in the single dipole case to make a two-level approximation for each dipole leads to the Dicke model (DM) in case of the Coulomb gauge

$$H_{\mathrm{DM}} = \hbar\tilde{\omega}_c c^\dagger c + \hbar\omega_{10} S_z + \hbar g_C (c + c^\dagger) S_x - \frac{\hbar\omega_c - \hbar\tilde{\omega}_c}{2}, \tag{1.33}$$

where $\tilde{\omega}_c = \tilde{\omega}_c(N) = \sqrt{\omega_c^2 + ND^2}$ now depends on the number of dipoles, or the extended Dicke model (EDM) in case of the dipole gauge

$$H_{\mathrm{EDM}} = \hbar\omega_c a^\dagger a + \hbar\tilde{\omega}_{01} S_z + \hbar g_D S_x (a^\dagger + a) + \frac{g_D^2}{\omega} S_x^2. \tag{1.34}$$

In the above equations the $S_j = \frac{1}{2}\sum_i \sigma_j^i$ denote collective spin matrices. The additional S_x^2 term in the EDM arises due to the aforementioned all-to-all coupling term and is also referred to as the P^2-term [23], in reference to the polarization operator. Making use of the Holstein-Primakoff approximation (see section 4.1) we can transform these Hamiltonians to exactly diagonalizable bilinear bosonic Hamiltonians (see section 4.2) and calculate the eigenmodes of the collective system, so-called polariton frequencies; in the Coulomb picture we obtain

$$\omega_{C\pm}^2 = \frac{1}{2}\left[\omega_{10}^2 + \tilde{\omega}_c^2 \pm \sqrt{(\tilde{\omega}_c^2 - \omega_{10}^2)^2 + 4N g_C^2 \tilde{\omega}_c \omega_{10}}\right], \tag{1.35}$$

whereas in the dipole picture the frequencies are

$$\omega_{D\pm}^2 = \frac{1}{2}\left[\Omega_{10}^2 + \omega_c^2 \pm \sqrt{\left(\Omega_{10}^2 - \omega_c^2\right)^2 + 4N g_D^2 \tilde{\omega}_{10} \omega_c}\right], \tag{1.36}$$

with $\Omega_{10} = \sqrt{\tilde{\omega}_{10}(\tilde{\omega}_{10} + N g_D^2/\omega_c)}$.

Apart from the immediate question as to which model yields the correct polariton frequencies we would also like to resolve the existence of a superradiant phase transition. A phase transition will occur when one of the polariton modes becomes unstable, i.e. when the lower frequency hits zero. Moving on from this point to higher coupling strengths would lead to imaginary frequencies which is a clear indication of the inadequacy of the current description and hints at a new phase with a different ground state configuration. In the

two gauges the lower frequency hits zero when

$$Ng_C^2 = \tilde{\omega}_c(N)\omega_{10}, \tag{1.37}$$

$$Ng_D^2 = \Omega_{10}^2 \frac{\omega_c}{\tilde{\omega}_{10}}. \tag{1.38}$$

With an argumentation analogous to the one we used to derive bounds for the dimensionless coupling parameters ζ_C and ζ_D it can be shown that

$$\frac{Ng_C^2}{\tilde{\omega}_c(N)\omega_{10}} \leq \frac{ND^2}{\omega_c^2 + ND^2} < 1, \tag{1.39}$$

$$\frac{Ng_D^2}{\Omega_{10}^2(\omega_c/\tilde{\omega}_{10})} \leq \frac{ND^2}{\tilde{\omega}_{10}^2 + ND^2} < 1. \tag{1.40}$$

However, values larger than 1 would be required for the lower polariton mode to become unstable. Hence the superradiant phase transition takes place in neither the Coulomb picture nor the dipole picture. Or does it? Taking into account direct dipole-dipole interactions will lead to an additional term in both Hamiltonians, $\frac{g_D^2}{\omega_c}\epsilon S_x^2$, and, as is shown in [8], a suitable geometry can lead to values of ϵ smaller than zero for which a superradiant phase transition does occur in the dipole picture.

This still leaves the question which gauge is correct in the many-dipole case; of course, having done the analysis in the single-dipole case, we would expect the electric dipole gauge to be correct also in the case of many dipoles. There is, however, a way to check agreement explicitly in the case of $N \to \infty$, which is detailed in the full paper [20]. Here we will just give the overall idea: when a very large number of dipoles is coupled to the same oscillator each dipole has the same chance to absorb a given photon and the probability of the same dipole absorbing two photons goes to zero. This means that transitions between higher-lying dipole states can be neglected. Hence we can replace the dipoles with a set of harmonic oscillators, one for each excited state. The excitation number of each of these oscillators then corresponds to the number of dipoles in the respective state. This procedure is also known as N-level Holstein-Primakoff approximation [24, 25] and it leads again to a bilinear bosonic Hamiltonian which can be diagonalized. Unsurprisingly, the dipole gauge turns out to work better also in the many-dipole case.

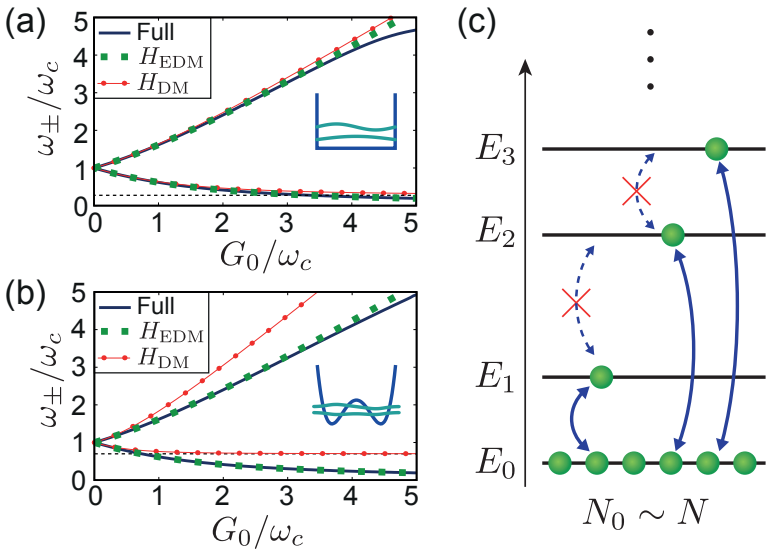

Figure 1.5: *Comparison of polariton eigenmodes of the full model (blue line), the Dicke model in the Coulomb gauge (red line) and the extended Dicke model in the dipole gauge (green line) for (a) the square-well and (b) the double-well potential. In both cases the EDM provides better results although in case of the double-well the differences between DM and EDM are much more pronounced. (c) Illustration of possible transitions in case of a large array of dipoles; since it is very unlikely for the same dipole to absorb two photons transitions between higher lying levels can be neglected and a multi-level Holstein-Primakoff approximation can be made, allowing for the derviation of the polariton eigenmodes in the full model.*

Chapter 2

Circuit-QED and the few dipole case

After having investigated the single-dipole case and the many-dipole case, both of which allow for the derivation of some analytic results, we would now like to turn our attention to the few-dipole case, which ultimately is the most relevant situation when it comes to experimental realizations and consequently tests of the theory. The more qubits one wants to control the more difficult a given setup will become to realize, hence the implementation of the many-qubit case will very likely be difficult. Although it would pose no bigger challenge to create a setup with a single qubit than to create one with a few qubits, the few-qubit case would allow for the observation of richer phenomenology; in particular it might be possible to observe the superradiant phase, given suitable inter-dipole interactions. While many physical systems exist which would in principle allow for an implementation of the quantum-optical models under consideration, superconducting circuits probably constitute the experimental platform where they can most readily be implemented with coupling strengths up to the USC regime. Whereas the considerations so far have been rather abstract, especially with the somewhat idealized double-well potential, in this section we are going to use realistic parameters for the constituents of our circuit. Predictions concerning the range of applicability of the two-state models will therefore be more meaningful.

2.0.1 Circuit-QED Hamiltonians

We are going to examine the superconducting circuit depicted in Fig.2.1 which comprises an LC-circuit and two flux qubits arranged in series. The circuit parameters (see below for definitions of the energies) are $E_{L_q}/h = 7$ GHz, $E_{C_q}/h = 12$ GHz and $E_J/h = 50$ GHz while E_{C_r} and E_{L_r} are chosen according to coupling strength in order to satisfy the

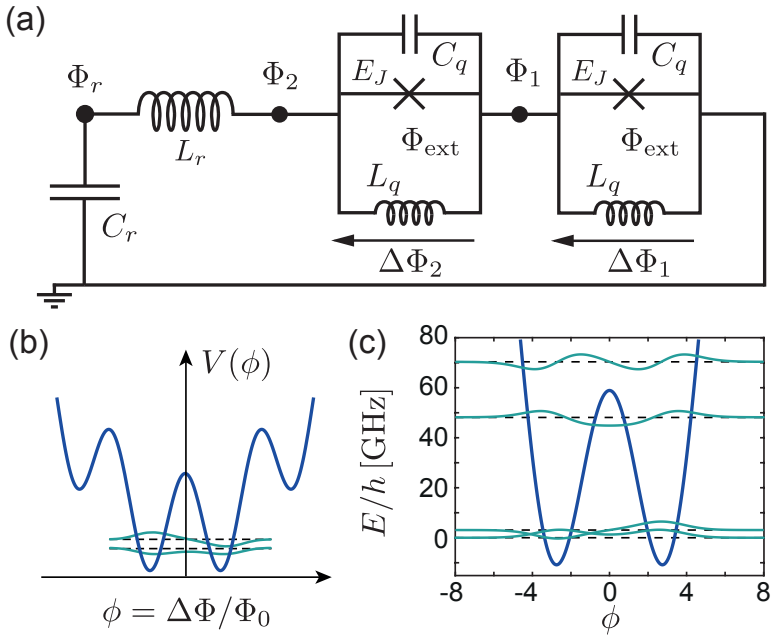

Figure 2.1: *Circuit QED with flux qubits. (a) Sketch of a multi-qubit circuit QED system, where two flux qubits are coupled to a lumped-element LC resonator with inductance L_r and capacitance C_r. In the simplest case, each flux qubit is realized by an rf-SQUID circuit and can be modeled as an effective particle with a dimensionless coordinate $\phi = \Delta\Phi/\Phi_0$ moving in an effective potential $V(\phi)$. (b) Typical shape of the potential $V(\phi)$ for a generic flux-qubit where the two lowest tunnel-coupled states form an isolated two-level subspace. (c) Shape of the potential $V(\phi)$ and the lowest eigenstates $|\varphi_n\rangle$ for a specific flux qubit with parameters $E_{L_q}/h = 7$ GHz, $E_{C_q}/h = 12$ GHz and $E_J/h = 50$ GHz.*

resonance-condition $\omega_c = \omega_{10}$. In the figure simple rf-SQUID circuits serve as our flux qubits, note, however, that this kind of circuit can also be used as an approximate model of e.g. the more elaborate Fluxonium qubit [26]. This is by no means the only setup that can (as we will show) be modeled by the (extended) Dicke model, see e.g. [1] for a circuit with charge instead of flux qubits.

A standard procedure on how to quantize superconducting circuits is given by Vool and Devoret in [27, 28] and we are going to illustrate the method for the example of our circuit: first, identify all nodes of the circuit, then introduce a set of generalized flux variables, so-called node fluxes, as

$$\Phi_\eta(t) = \int_{-\infty}^{t} ds\, V_\eta(s), \qquad \eta \in \{r, 1, 2\}, \tag{2.1}$$

where V_η is the voltage at the respective node. Remembering the well known classical equations, contributions to the overall energy of the system can be written in terms of the node fluxes: in case of capacitors the contribution is $CU^2/2 \to C\Delta\dot{\Phi}^2/2$, in case of inductances we get $\phi^2/2L \to \Delta\Phi^2/2L$, or, for the Josephson junction, which can be thought of as a nonlinear inductance, the relation is $-E_J \cos\left(\frac{\Delta\Phi_i + \Phi_{\text{ext}}}{\Phi_0}\right)$ (where $\Phi_0 = \hbar/2e$ is the reduced flux quantum). The kinetic, or capacitive, energy of the system then becomes

$$T = \frac{C_r \dot{\Phi}_r^2}{2} + \sum_{i=1}^{N} \frac{C_q (\Delta\dot{\Phi}_i)^2}{2}, \tag{2.2}$$

whereas the potential, or inductive, energy is given by

$$V_{\text{tot}} = \frac{(\Phi_r - \Phi_2)^2}{2L_r} + \sum_{i=1}^{N} \left[\frac{(\Delta\Phi_i)^2}{2L_q} - E_J \cos\left(\frac{\Delta\Phi_i + \Phi_{\text{ext}}}{\Phi_0}\right)\right]. \tag{2.3}$$

The $\Delta\Phi$ denote phase jumps across the corresponding circuit element. From this we can easily write down the Lagrangian of the system, $\mathcal{L} = T - V_{\text{tot}}$, and calculate the corresponding canonical momenta, to be interpreted as charges, via $Q_r = \partial\mathcal{L}/\partial\dot{\Phi}_r = C_r\dot{\Phi}_r$, and $Q_i = \partial\mathcal{L}/\partial\Delta\dot{\Phi}_i = C_q\Delta\dot{\Phi}_i$. Now, following the common procedure of canonical quantization and after introducing new, dimensionless variables $\phi_r = \Phi_r/\Phi_0$, $\phi_i = \Delta\Phi_i/\Phi_0$ and $\mathcal{Q}_\eta = Q_\eta/(2e)$, we promote them to quantum mechanical operators by imposing commutation relations $[\phi_\eta, \mathcal{Q}_{\eta'}] = i\delta_{\eta,\eta'}$. Switching from Lagrangian to Hamiltonian picture then

yields the circuit Hamiltonian

$$H_\Phi = 4E_{C_r}\mathcal{Q}_r^2 + \frac{E_{L_r}}{2}\left(\phi_r - \sum_{i=1}^{N}\phi_i\right)^2 + \sum_{i=1}^{N}\left[4E_{C_q}\mathcal{Q}_i^2 + E_J\cos(\phi_i) + \frac{E_{L_q}}{2}\phi_i^2\right], \tag{2.4}$$

where we have defined the inductive energies $E_{L_\eta} = \Phi_0^2/L_\eta$ and, following the usual convention, the capacitive energies $E_{C_\eta} = e^2/(2C_\eta)$. Introducing creation and annihilation operators to simplify the description of the LC-part of the circuit we can write $\phi_r = \sqrt[4]{2E_{C_r}/E_{L_r}}(a^\dagger + a)$ and $\mathcal{Q}_r = i\sqrt[4]{E_{L_r}/32E_{C_r}}(a^\dagger - a)$. Identifying ϕ_i and $\mathcal{Q}_i$ with the coordinate and momentum of an effective particle moving in a potential $V(\phi_i) = E_J\cos(\phi_i) + E_{L_q}\phi_i^2/2$ we see that the circuit elements constituting our flux qubits can indeed be seen as artificial atoms and we recognize that Hamiltonian H_Φ is identical to Hamiltonian H_D in the dipole gauge. After making a two-level approximation we obtain the extended Dicke model

$$H_{\mathrm{EDM}}^{\Phi} = \hbar\omega_c a^\dagger a + \hbar\tilde{\omega}_{01}S_z + \hbar g_D S_x(a^\dagger + a) + \frac{g_D^2}{\omega_c}S_x^2, \tag{2.5}$$

with $\omega_c = \sqrt{8E_{C_r}E_{L_r}}/\hbar$ and $g_D = \omega_c\left(\frac{E_{L_r}}{2E_{C_r}}\right)^{\frac{1}{4}}|\langle\tilde{\varphi}_0|\phi|\tilde{\varphi}_1\rangle|$.

To get the circuit-QED equivalent of the Coulomb picture we can utilize the unitary transformation $U = e^{-i\mathcal{Q}_r\sum_i\phi_i}$ to calculate $H_Q = UH_\Phi U^\dagger$ and obtain

$$H_Q = 4E_{C_r}\mathcal{Q}_r^2 + \frac{E_{L_r}}{2}\phi_r^2 + \sum_i\left[4E_{C_q}(\mathcal{Q}_i - \mathcal{Q}_r)^2 + V(\phi_i)\right], \tag{2.6}$$

or, after performing the TLA, the Dicke model

$$H_{\mathrm{DM}}^{Q} = \hbar\tilde{\omega}_c c^\dagger c + \hbar\omega_{10}S_z + \hbar g_C(c + c^\dagger)S_x - \frac{\hbar\omega_c - \hbar\tilde{\omega}_c}{2}, \tag{2.7}$$

where $\tilde{\omega}_c = \sqrt{8(E_{C_r} + NE_{C_q})E_{L_r}}/\hbar$ and $g_C = \frac{8E_{C_q}}{\hbar}\sqrt{\frac{\omega_c}{\tilde{\omega}_c}}\left(\frac{E_{L_r}}{2E_{C_r}}\right)^{\frac{1}{4}}|\langle\varphi_0|\mathcal{Q}|\varphi_1\rangle|$. Hence we have shown that the circuit-QED setup presented in this section is formally equivalent to the cavity-QED setup considered before.

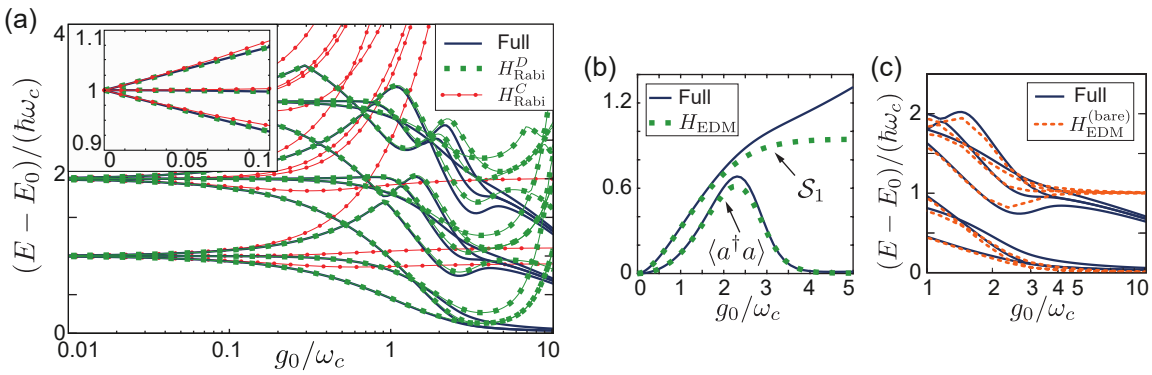

Figure 2.2: *(a) Energy spectrum of a superconducting circuit containting two flux-qubits (see Fig. 2.1) where the blue line corresponds to the full Hamiltonian, the green one to the Φ-interaction/dipole EDM and the red line to the Q-interaction/Coulomb DM. We observe that in the dipole gauge we obtain very good results up to coupling strengts $g_0/\omega_c \approx 3$, especially for the lower energy levels. (b) The single-qubit entanglement entropy and expectation value of the photon number in the ground state are depicted; this shows that characteristic USC effects like decoupling between cavity and qubits or the transition to an entangled subradiant ground state are also captured by the two-state model. (c) Alternative treatment of the x^2 (Φ^2) term by simply omitting it instead of including it in the atomic Hamiltonian. Qualitative features of the spectrum for large g_0 are captured better that way.*

2.0.2 Comparison

Finally, we can again compare the predictions of the 2-state Hamiltonians to those of the full model; since, this time, the parameters of our approximate models are derived from a rather realistic setup, more weight can be given to the apparent range of validity of the TLA.

As can be seen from the spectrum depicted in Fig. 2.2 (a) results are very similar to those received in section 1.3 for the highly anharmonic double-well: the Coulomb gauge fails early at coupling strengths of $g_0/\omega_c \approx 0.1$, whereas the dipole gauge provides much better results and remains valid up to $g_0/\omega_c \approx 3$, where deviations from the full model become more pronounced. The smaller range of agreement in the dipole picture follows from the fact that the double-well potential at hand has an anharmonicity of just $\Delta_{nl} \approx 15$, much lower than that of the double-well considered previously. Fig. 2.2 (b) shows that magnitudes like the single-qubit entanglement entropy and the photon number in the ground state also show the behaviour typical of USC: the single-qubit entanglement entropy approaches the value of two-maximally entangled qubits demonstrating decoupling between cavity and the collective

qubit-subsystem whereas the expectation value of the photon number reapproaches zero after an inital ascent, indicating the transition to a subradiant ground state [8]. Finally, in Fig. 2.2 (c) we investigate how to best deal with the x^2 term which we have, so far, included in the atomic potential; if we keep it outside where (in the TLA) the term becomes constant (since $\sigma_x^2 = 1$) we observe that, while there is no significant change in the range of agreement, the qualitative features of the spectrum like the emergence of 2^N-fold degenerate manifolds are captured much better that way.

Conclusions

We have demonstrated the importance of carefully choosing the correct gauge when deriving effective light-matter Hamiltonians. We have compared the results obtained in the Coulomb gauge and those obtained in the electric dipole gauge and shown that the dipole gauge provides more accurate results. The main reason for the validity of the two-level approximation in the dipole gauge and its invalidity in the Coulomb gauge is to be found in the different matrix transition elements of the operators involved in the coupling. These results also resolve the controversies about the Dicke model in form of the contradictory no-go- and counter no-go-theorem. Finally, we have shown that the correct effective Hamiltonian is suitable to describe a realistic superconducting-circuit setup in the USC regime.

Part II

Thermodynamics of cavity QED

Chapter 3

Phase transitions in the EDM

In this chapter we are going to review the various phase transitions that are known to occur in the extended Dicke model for $\epsilon \in [-1, 1]$ and for coupling strengths $g \in [0, \infty)$. From now on we will set $\hbar = 1$; nevertheless, for the sake of clarity, we are still going to write down the $\hbar$ explicitly in some expressions like e.g. the labels of plots or expressions containing other physical constants. First, let us write down the Hamiltonian of the full EDM:

$$H_{\mathrm{EDM}} = \omega_c a^\dagger a + \omega_{qb} S_z + g(a^\dagger + a) S_x + \frac{g^2}{\omega_c}(1 + \epsilon) S_x^2. \tag{3.1}$$

Note, that unlike in the previous part, where we neglected direct dipole-dipole interactions, we have now included these interactions in an approximate way, by replacing the real interactions by a corresponding all-to-all coupling.

The groundstate of the extended Dicke model is known to exhibit three different phases in different parameter regimes; see e.g. [8] for the ground state phase diagram. For weak coupling strengths g the system is in the normal phase. The characteristics of this phase can easily be seen by considering the EDM Hamiltonian in the limit $g \to 0$:

$$\lim_{g \to 0} H_{\mathrm{EDM}} = \omega_c a^\dagger a + \omega_{qb} S_z. \tag{3.2}$$

In order to minimize the ground state energy there cannot be any photons and all spins must be aligned in negative z-direction, hence we find $\langle S_z \rangle = -N_{qb}/2$.

As the coupling strength increases a transition to two other phases is possible: in case of $\epsilon < 0$ a second order phase transition to the superradiant phase occurs. In this phase

the expectation values of the photonic annihilation operator a and the spin-x component S_x exhibit non-zero values. In case of $\epsilon > 0$ a cross-over to the so-called subradiant phase takes place. The spins anti-align, leading to spin-expectation values $\langle S_k \rangle = 0$ and cavity excitations disappear from the ground state. In addition to these two phase transitions a third one exists, namely a first-order transition between subradiant and superradiant phase. In this section we are going to investigate how the sub- and superradiant phase transitions change at finite temperatures.

3.1 The canonical ensemble

First, we would like to clarify what exactly we mean when we are talking about the thermal state of the system and how we calculate expectation values at finite temperatures. We assume that our system, which is described by the extended Dicke model, is in contact with a much larger heat bath. Our system and the bath can exchange energy and since the bath is much larger the system will equilibrate with the temperature of the bath. No particles can be exchanged. Therefore, we can use the canonical ensemble to describe the thermal properties of our system.

To calculate thermal expectation values we proceed by first calculating the partition function of the system

$$Z_K = \sum_{k=0}^{n} m_{\epsilon_k} e^{-\beta \epsilon_k} \tag{3.3}$$

by adding up the Boltzmann factors of all energy levels where m_{ϵ_k} is the degeneracy of a given state and $\beta = 1/k_B T$; k_B denotes the Boltzmann constant and $n+1$ refers to the number of different states. In the DM and the EDM n becomes infinite. In section 7.2 we are going to detail how the EDM-Hamiltonian can be split up into smaller blocks and how the degeneracy of the resulting eigenstates can be determined. Next, we form the density matrix

$$\rho_{th} = \frac{1}{Z_K} \sum_{k=0}^{n} m_{\epsilon_k} e^{-\beta \epsilon_k} \left|\psi_{\epsilon_k}\right\rangle \left\langle\psi_{\epsilon_k}\right|, \tag{3.4}$$

which we can utilize to calculate expectation values of operators

$$\langle \hat{O} \rangle = Tr\{\rho_{th} \hat{O}\} = \frac{1}{Z_K} \sum_{k=0}^{n} m_{\epsilon_k} e^{-\beta \epsilon_k} \left\langle \psi_{\epsilon_k} | \hat{O} | \psi_{\epsilon_k} \right\rangle. \tag{3.5}$$

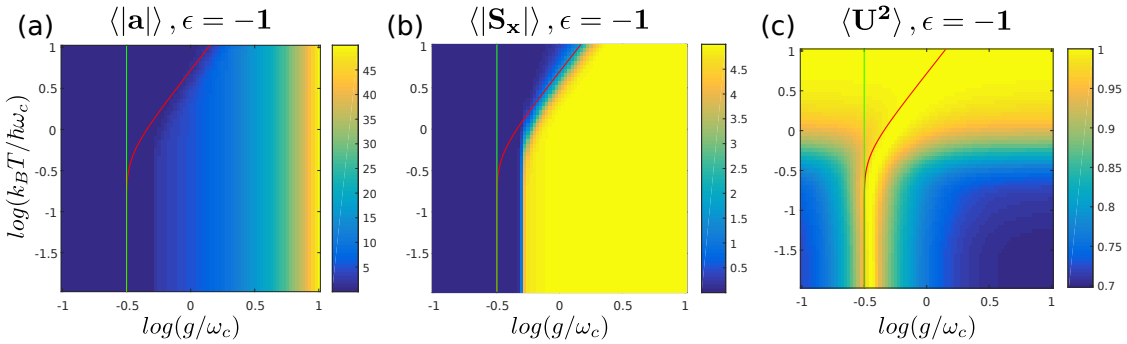

Figure 3.1: *Superradiant phase transition ($\epsilon = -1$, $N_{qb} = 10$): The thermal average of the absolute value of the expectation values of (a) the annihilation operator and (b) the x-component of the collective spin as well as (c) the expectation value of the U^2-term are depicted for temperatures kT between 0.01 and 10 and for coupling strengths ranging from weak coupling to USC. The U^2 values are normalized to their respective maximum value at a given temperature. For low temperatures, the onset of the superradiant phase transition, characterized by non-zero expectation values of the operators under consideration, is clearly visible. As we move to higher temperatures we observe that the onset of the phase transition is delayed to higher coupling strengths and that the transition itself is smeared over a wider range of coupling strengths; in case of the U^2-operator the transition becomes almost unidentifiable. The red line indicates the critical temperature at which the superradiant phase vanishes as predicted by mean field theory. Despite the rather crude nature of the approximation as well as a qubit number of only $N_{qb} = 10$ the mean field approximation provides very accurate results. The green line corresponds to the critical coupling strength as predicted by the Holstein Primakoff approximation; in contrast to MFT it is independent of temperature.*

Hence, given the eigenenergies and the eigenstates of the extended Dicke model, we can calculate thermal properties.

3.2 Superradiant phase transition for $\epsilon < 0$

First, we are going to take a look at the superradiant phase transition. In the ground state it is most easily characterized by the non-vanishing expectation values of the a- and S_x-operators. For finite temperatures, however, things get a bit more tricky. For each state with expectation values $\langle a\rangle$, $\langle S_x\rangle$ a state of (almost) equal energy but expectation values of opposite sign exists; this means, that the thermal average of these expectation values will always be zero. One way to circumvent this problem is to take a look a the thermal average

over the absolute value of these expectation values, i.e. we calculate

$$\langle|\hat{O}|\rangle := \frac{1}{Z_K}\sum_{k=0}^{n} m_{\epsilon_k} e^{-\beta\epsilon_k} |\langle\psi_{\epsilon_k}|\hat{O}|\psi_{\epsilon_k}\rangle|. \tag{3.6}$$

While these expectation values are not directly measurable, they provide a useful means of visualizing the phase transition. In our numerical simulations we have added a small symmetry-breaking bias field in order to be able to reliably address states with expectation values of the same sign.

In figure 3.1 (a) and (b) we have plotted the expectation values of these operators for coupling strengths ranging from weak coupling to ultrastrong coupling and for a range of temperatures corresponding to thermal energies from well below the cavity/qubit frequency to well above. The onset of the superradiant phase transition is clearly identifiable in both cases, although the S_x-expectation values provide a more precise understanding; while $\langle a\rangle$ is going to rise indefinitely $\langle S_x\rangle$ will approach its maximum value $N_{qb}/2$, hence the phase transition can be taken as completed once the expectation value is sufficiently close to the maximal value. Hence, judging by the S_x-plot, we observe a very sharp transition at low temperatures, whereas at high temperatures it takes higher couplings strengths for the SRT to start and the transition itself is smeared out over a broader range of coupling strengths.

The red line, which is visible in the plots, depicts the critical coupling strength as calculated by mean field theory. The green line corresponds to the prediction made by Holstein Primakoff, which remains constant for all temperatures; it is in agreement with MFT for low temperatures. The MFT prediction captures the overall characteristics very well: the critical coupling strength doesn't change much at low temperatures but as soon as the thermal energy becomes comparable to the frequencies involved in the EDM it bends to the right, in agreement with the expectation values. For low temperatures, MFT predicts a smaller value for g_c than the expectation values would imply, for higher temperatures the difference becomes less and in case of the S_x-expectation value the line appears to be located very nicely in the middle of the transition.

Furthermore, we have plotted a third quantity in figure 3.1 (c), the fluctuations of the operator

$$U = \frac{1}{\sqrt{2}}\left(a + a^\dagger + \frac{2g}{\omega_c}S_x\right). \tag{3.7}$$

Depending on which setup the EDM refers to, this operator can have different interpre-

tations. In case of the circuit in figure 2.1 it is proportional to the current through the upper part of the circuit whereas in the setup considered in [8], where dipoles are inside of a capacitor, it refers to the voltage across the capacitor. At a given temperature, values are normalized to the respective maximum. At low temperatures, the peak is clearly visible and starts to bend towards higher coupling strengths for higher temperatures. As we approach higher temperatures, the peak becomes less and less pronounced, due to the fact that fluctuations induced by the coupling between cavity and qubits now constitute only a minor contribution to the U^2-expectation value and thus the overall energy of the system. It is remarkable that the MFT prediction of the critical coupling strength very closely follows the peak of this observable, for both low and high temperatures.

3.3 Subradiant phase for $\epsilon > 0$

For values $\epsilon > 0$ a crossover to the subradiant state takes place, which is best characterized by the number of photons present in the system. Figure 3.2 depicts the photon number expectation value, in the same range of coupling strengths and temperatures as before; the expectation values are again normalized to their respective maximum at a given temperature. We can clearly observe an initial increase of the photon number followed by a subsequent decrease to the inital value, which is zero in case of zero temperature. For higher temperatures we observe a 'background'-photon number due to the non-zero thermal energy but on top of this the characteristics of the subradiant phase transition can still be observed. Like before in the SRT, as we approach higher temperatures, the phase transition moves towards higher coupling strengths. This time, however, a broadening of the phase transition cannot be observed, at least not from the parameters under consideration.

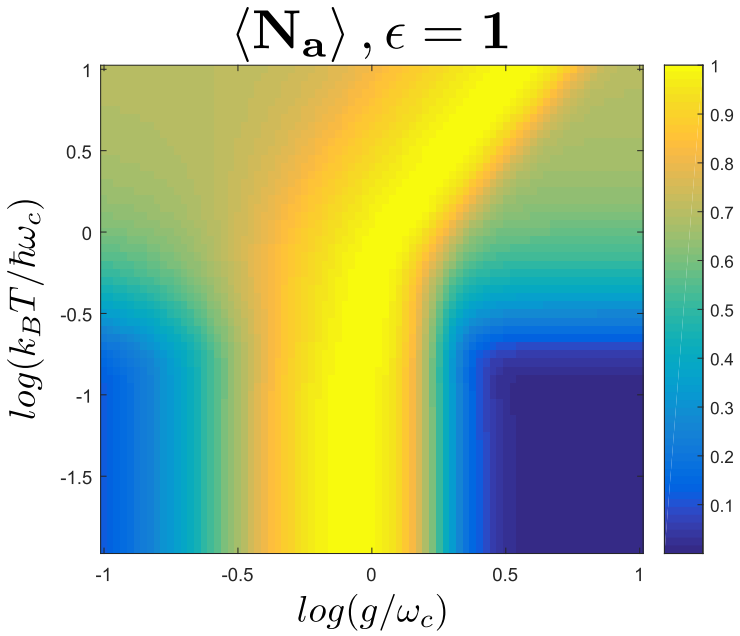

Figure 3.2: *Subradiant phase ($\epsilon = 1$, $N_{qb} = 10$): A decline of the mean photon number at large coupling strengths, following an inital rise, is characteristic of the crossover to a subradiant phase which takes place for $\epsilon > 0$. Here we have depicted this expectation value for temperatures between 0.01 and 10, where, at a given temperature, we have normalized the values to their respective maximum in order to highlight the main features of the plot (otherwise, high values at higher temperatures would make features in the low-temperature regime unrecognizable). At low temperatures, the emergence of the subradiant phase is clearly visible, from the maximum of the photon number $\langle N_a \rangle$. As the temperature increases we find a certain amount of 'background-photons' that are always there, irrespective of coupling; the phase transition still exists but it starts at higher coupling strengths.*

Chapter 4

The EDM in the Holstein - Primakoff approximation

Let us, for the sake of clarity, write down again the Hamiltonian of the full extended Dicke model:

$$H_{\mathrm{EDM}} = \omega_c a^\dagger a + \omega_{qb} S_z + g(a^\dagger + a)S_x + \frac{g^2}{\omega_c}(1+\epsilon)S_x^2. \tag{4.1}$$

In this section we are going to bosonize the spin part of the extended Dicke model by employing the well-known Holstein-Primakoff approximation; this procedure yields a bilinear bosonic Hamiltonian which is exactly diagonalizable (see section 4.2) and therefore allows for the derivation of analytic results. Emary and Brandes have used the HP approximation in their study of 'Chaos and the Quantum Phase Transition in the Dicke Model' [7] and here we will extend their derivation of the Dicke model Holstein-Primakoff Hamiltonian to the extended Dicke model. Furthermore, we are going to calculate expectation values of the HP model and compare them to those of the full model to assess the validity of the approximation.

4.1 The Holstein - Primakoff transformation

Holstein and Primakoff first introduced the eponymous transformation in their 1940 paper 'Field Dependence of the Intrinsic Domain Magnetiaztion of a Ferromagnet' [29]. It is a method to express spin operators in terms of bosonic creation and annihilation operators. The first hint on how such a transformation might look like is given by the action of spin

operators on the corresponding quantum states:

$$S^2 |S,m\rangle = S(S+1) |S,m\rangle , \tag{4.2}$$

$$S_z |S,m\rangle = m |S,m\rangle , \tag{4.3}$$

$$S_\pm |S,m\rangle = \sqrt{S(S+1) - m(m\pm 1)} |S,m\pm 1\rangle . \tag{4.4}$$

These relations, as well as the commutation relations

$$[S_i, S_j] = i\epsilon_{ijk} S_k \tag{4.5}$$

and

$$[S_+, S_-] = 2S_z, \tag{4.6}$$

have to be reproduced by the new operators. Taking the state $|S,-S\rangle := |0\rangle$ as the bosonic vacuum state, such that $|S,-S+n\rangle = \frac{1}{\sqrt{n!}}(a^\dagger)^n |0\rangle$, we can write the spin operators as

$$S_+ = a^\dagger \sqrt{2S}\sqrt{1 - \frac{a^\dagger a}{2S}}, \tag{4.7}$$

$$S_- = \sqrt{2S}\sqrt{1 - \frac{a^\dagger a}{2S}}\, a, \tag{4.8}$$

$$S_z = (a^\dagger a - S). \tag{4.9}$$

Inserting these operators into the above relations and making use of the bosonic commutation relation $[a, a^\dagger] = 1$ as well as the action of the number operator $a^\dagger a |n\rangle = n |n\rangle$ the correctness of this ansatz can readily be shown.

The main reason for the usefulness of this transformation lies in the fact that when the bosonic excitation number is small when compared to the total spin, i.e. when the magnetic quantum number is near its minimum or $\langle a^\dagger a\rangle \ll S$, the square root $\sqrt{1 - \frac{a^\dagger a}{2S}}$ can conveniently be approximated as 1. Therefore, in the Holstein-Primakoff approximation, the spin-operators can be written as

$$S_+ \approx \sqrt{2S}a^\dagger, \tag{4.10}$$

$$S_- \approx \sqrt{2S}a, \tag{4.11}$$

$$S_x \approx \frac{\sqrt{2S}}{2}(a + a^\dagger), \tag{4.12}$$

$$S_y \approx i\frac{\sqrt{2S}}{2}(a - a^\dagger). \tag{4.13}$$

These operators are much less unwieldy than the full spin operators and, when inserted into the Hamiltonian of the extended Dicke model, lead to a bilinear bosonic Hamiltonian. It is important to keep in mind that $\langle a^\dagger a\rangle \ll S$ must be fulfilled in order for this method to work; this will be important when the EDM enters the superradiant phase and will force us to shift our bosonic operators when performing the HP approximation.

4.2 On the diagonalization of a general bilinear bosonic Hamiltonian

Before turning our attention to the actual bosonization of the EDM Hamiltonian, let us quickly review two different methods of diagonalizing a bilinear bosonic Hamiltonian. Results derived in this section will be directly applicable to the HP Hamiltonians derived in succeeding sections.

4.2.1 Method of Tsallis

First, we are going to briefly summarize a method which was introduced by Tsallis in his paper 'Diagonalization methods for the general bilinear Hamiltonian of an assembly of bosons' [30] and which is equivalent to the so-called equation of motion (EOM) approach (see e.g. [31]). We start out with the general bilinear Hamiltonian of N bosonic modes (with $[b_i, b_i^\dagger] = 1, \dots$) and, neglecting constant contributions, we can write

$$\mathcal{H} = \sum_{i=1}^{N}\sum_{j=1}^{N} 2\omega_{ij} b_i^\dagger b_j + \nu_{ij} b_i^\dagger b_j^\dagger + \nu_{ij}^\star b_i b_j = \sum_{i=1}^{N}\sum_{j=1}^{N} \omega_{ij} b_i^\dagger b_j + \omega_{ij}^\star b_i b_j^\dagger + \nu_{ij} b_i^\dagger b_j^\dagger + \nu_{ij}^\star b_i b_j \tag{4.14}$$

$$= \vec{b} H \vec{b}^T \stackrel{!}{=} \vec{B} H_D \vec{B}^T = \sum_{j=1}^{N} 2\Omega_j B_j^\dagger B_j,$$

where $\vec{b} = [b_1^\dagger \dots b_N^\dagger b_1 \dots b_N]$ and

$$H = \begin{bmatrix} \omega & \nu \\ \nu^\star & \omega^\star \end{bmatrix}, \tag{4.15}$$

$$H_D = \begin{bmatrix} \Omega & 0_N \\ 0_N & \Omega, \end{bmatrix}, \tag{4.16}$$

where Ω contains the Ω_j as diagonal elements. The goal is to find a transformation matrix T that lets us switch between the two pictures; this transformation has to deliver both a diagonal H_D and keep the bosonic commutation relations intact. Defining T via

$$\vec{B}^T = T^\dagger \vec{b}^T, \tag{4.17}$$

$$\vec{B} = \vec{b} T, \tag{4.18}$$

we can write

$$\mathcal{H} = \vec{b}(TT^{-1})H(J(T(JJ)T^{-1})J)\vec{b}^T, \tag{4.19}$$

where

$$J = \begin{bmatrix} 1_N & 0_N \\ 0_N & -1_N \end{bmatrix}. \tag{4.20}$$

Tsallis shows that the matrix T must have the properties

$$T^\dagger J T J = 1_{2N}, \tag{4.21}$$

$$T^{-1} H J T = H_D J. \tag{4.22}$$

The additional matrix J is necessary to account for the bosonic commutation relations.

Hence T can be found by taking the following steps: find the matrix T_0 that diagonalizes HJ to fulfill (4.22); then the columns of T_0 (i.e. the eigenvectors) can be normalized seperately to satisfy (4.21):

$$\vec{T_{0j}}^{\dagger} J \vec{T_{0j}} = J_{jj}. \tag{4.23}$$

Attention must be paid to the ordering of the eigenvectors, i.e. $j \in \{1, \ldots, N\}$ correspond to the new annihilation operators b_j whereas $j \in \{n+1, \ldots, 2N\}$ correspond to the respective creation operators $b_j^{\dagger}$.

Although we will use a different method to derive analytic results we have used this approach to cross-check our results numerically. As we shall see, one advantage of the diagonalization scheme discussed in the next section lies in the facts that new quantities, the use of which greatly simplifies the resulting formulas, naturally arise in the course of the derivation. Furthermore, it will be possible to simply read energies off an equation instead of having to solve an eigenvalue problem.

4.2.2 Diagonalization in the position-momentum picture

While the above method already is general it can often be easier to switch to a position-momentum picture via the harmonic oscillator relations

$$x = \sqrt{\frac{1}{2\omega}}(a^{\dagger} + a), \tag{4.24}$$

$$p = i\sqrt{\frac{\omega}{2}}(a^{\dagger} - a). \tag{4.25}$$

Inverting these relations we can find expressions for $a^{\dagger}$ and a in terms of x and p. The number operator $a^{\dagger}a$ can then be expressed as

$$\omega a^{\dagger} a = \frac{1}{2}(\omega^2 x^2 + p^2 - \omega) \tag{4.26}$$

and inserting the relations into a bilinear bosonic Hamiltonian will lead to an expression of the form

$$H = \sum_i \sum_j a_{ij} x_i x_j + b_{ij} p_i p_j + c_{ij} x_i p_j + const. \tag{4.27}$$

Now, the idea is to rotate the coordinate system in a way such that terms with $i \neq j$ and cross-terms between position and momentum operators vanish. Of course this approach

is not necessarily easier than the previous method but as we will see it works well for the Hamiltonians that we are going to consider.

We will now demonstrate this method using the example of a Hamiltonian which has the same overall form as the HP-Hamiltonians we are going to derive in the following sections. We consider the Hamiltonian

$$H = \omega_0 c^\dagger c + \omega_1 d^\dagger d + (\kappa + f_\epsilon)(d^\dagger + d)^2 + h(c^\dagger + c)(d^\dagger + d) \tag{4.28}$$

which can be rewritten in the position-momentum picture as

$$H = \frac{1}{2}\left(\omega_0^2 x^2 + p_x^2 + \omega_1^2 y^2 + p_y^2 + 4\omega_1(\kappa + f_\epsilon)y^2 + 4h\sqrt{\omega_0\omega_1}xy - \omega_0 - \omega_1\right), \tag{4.29}$$

where we have introduced the new position and momentum operators

$$\begin{aligned} x &= \frac{1}{2\epsilon_+}(c^\dagger + c), \qquad p_x = i\frac{\epsilon_+}{2}(c^\dagger - c), \\ y &= \frac{1}{2\epsilon_-}(d^\dagger + d), \qquad p_y = i\frac{\epsilon_-}{2}(d^\dagger - d). \end{aligned} \tag{4.30}$$

Next, we rotate our coordinate system by an angle γ such that the old coordinates x and y can be expressed in terms of the new coordinates X and Y as

$$\begin{aligned} x &= X\cos(\gamma) + Y\sin(\gamma), \qquad p_x = P_X\cos(\gamma) + P_Y\sin(\gamma), \\ y &= -X\sin(\gamma) + Y\cos(\gamma), \qquad p_y = -P_X\sin(\gamma) + P_Y\cos(\gamma). \end{aligned} \tag{4.31}$$

Any arbitrary 2D-rotation can be effected that way by choosing γ accordingly. The Hamiltonian in terms of the rotated coordinates becomes

$$\begin{aligned} H = \frac{1}{2}\big[&X^2\left(\omega_0^2\cos^2(\gamma) + \omega_1^2\sin^2(\gamma) + 4\omega_1(\kappa + f_\epsilon)\sin^2(\gamma) - 2h\sqrt{\omega_0\omega_1}\sin(2\gamma)\right) + P_X^2 \\ &+Y^2\left(\omega_0^2\sin^2(\gamma) + \omega_1^2\cos^2(\gamma) + 4\omega_1(\kappa + f_\epsilon)\cos^2(\gamma) + 2h\sqrt{\omega_0\omega_1}\sin(2\gamma)\right) + P_Y^2 \\ &+XY\left(\omega_0^2\sin(2\gamma) - \omega_1^2\sin(2\gamma) - 4\omega_1(\kappa + f_\epsilon)\sin 2\gamma + 4h\sqrt{\omega_0\omega_1}\cos(2\gamma)\right) - \omega_0 - \omega_1\big]. \end{aligned} \tag{4.32}$$

Requiring that the XY term vanish delivers an equation allowing us to determine γ:

$$\tan(2\gamma) = \frac{4h\sqrt{\omega_0\omega_1}}{\omega_1^2 + 4\omega_1(\kappa + f_\epsilon) - \omega_0^2}. \tag{4.33}$$

Comparing this Hamiltonian to the expression (4.26) we can read off the new oscillator frequencies and by using the relation derived for γ as well as some trigonometric identities, the resulting expressions can be simplified to

$$\epsilon_\pm^2 = \frac{1}{2}\left[\omega_0^2 + \omega_1^2 + 4\omega_1(\kappa + f_\epsilon) \pm \sqrt{(\omega_0^2 - \omega_1^2 - 4\omega_1(\kappa + f_\epsilon))^2 + 16h^2\omega_0\omega_1}\right]. \tag{4.34}$$

Switching again to creation and annihilation operators via

$$\begin{aligned} X &= \frac{1}{2\epsilon_+}(c_+^\dagger + c_+), \qquad P_X = i\frac{\epsilon_+}{2}(c_+^\dagger - c_+), \\ Y &= \frac{1}{2\epsilon_-}(c_-^\dagger + c_-), \qquad P_Y = i\frac{\epsilon_-}{2}(c_-^\dagger - c_-), \end{aligned} \tag{4.35}$$

H can be written in terms of the bosonic operators corresponding to the eigenenergies

$$H = \epsilon_+ c_+^\dagger c_+ + \epsilon_- c_-^\dagger c_- + \frac{1}{2}(\epsilon_+ + \epsilon_- - \omega - \omega_1). \tag{4.36}$$

Note, that by utilizing (4.30), (4.31) and (4.35) the coefficients to express c, d in terms of c_+, c_- and vice versa can easily be determined.

4.3 Normal phase

Having reviewed the underlying techniques we can now start with the bosonization of the EDM. For weak coupling strengths the system is in the normal phase, where the spins are all aligned in negative z-direction to result in the minimal magnetic quantum number and where $\langle a \rangle$ and $\langle S_x \rangle$ are still 0. Hence the bosonization procedure is straightforward and we can replace the spin operators in H_{EDM} with the expressions derived in section 4.1:

$$S_x = \frac{\sqrt{2S}}{2}(b^\dagger + b), \tag{4.37}$$

$$S_z = (b^\dagger b - S). \tag{4.38}$$

Plugging these equations into H_{EDM} yields

$$H_{HP}^{n} = \omega_{qb}(b^\dagger b - S) + g'(b^\dagger + b)(a^\dagger + a) + \frac{g'^2}{\omega_c}(1+\epsilon)(b+b^\dagger)^2 + \omega_c a^\dagger a, \tag{4.39}$$

where $g' = g\frac{\sqrt{2S}}{2}$. Comparing H_{HP}^{n} to Hamiltonian (4.28), which we explicitly diagonalized in section 4.2.2, we can identify the correspondences $\omega_0 \leftrightarrow \omega_c$, $\omega_1 \leftrightarrow \omega_{qb}$, $h \leftrightarrow g'$, $\kappa \leftrightarrow g'^2/\omega_c$ and $f_\epsilon\epsilon \leftrightarrow g'^2/\omega_c$. Therefore, we can rewrite H_{HP}^{n} as

$$H_{HP}^{n} = \omega_+ c_+^\dagger c_+ + \omega_- c_-^\dagger c_- + C, \tag{4.40}$$

with

$$C = -\omega_{qb}S - \frac{\omega_{qb} - \tilde{\omega}_{qb}}{2} + \frac{1}{2}(\omega_+ + \omega_- - \omega_c - \tilde{\omega}_{qb}), \tag{4.41}$$

$$\omega_\pm^2 = \frac{1}{2}\left[\omega_c^2 + \Omega^2 \pm \sqrt{(\omega_c^2 - \Omega^2)^2 + 16g^2\omega_c\omega_{qb}}\right], \tag{4.42}$$

where $\Omega^2 = \omega_{qb}^2 + \frac{4\omega_{qb}g'^2}{\omega_c}(1+\epsilon)$. Hence we have found a way to approximately describe the extended Dicke model in the normal phase in terms of two decoupled harmonic oscillators.

Being aware of the fact that in the EDM, depending on the value of ϵ, two different phase transitions are possible we are now going to investigate whether these phase transitions are part of the approximate model as well. A way to identify a phase transition is to look at the eigenmode ω_- and determine whether a ground state-instability occurs, i.e. whether a g_c exists for which ω_- becomes zero; this would imply unphysical imaginary frequencies for coupling strengths $g > g_c$ and hence a breakdown of our model. The condition $\omega_- = 0$ leads to the equation

$$\omega_c^2 + \Omega^2 = \sqrt{(\omega_c^2 - \Omega^2)^2 + 16g_c^2\omega_c\omega_{qb}} \tag{4.43}$$

and solving for g_c we obtain

$$g_c = \sqrt{\frac{\omega_c\omega_{qb}}{-N\epsilon}}. \tag{4.44}$$

Hence for values of $\epsilon < 0$ a (real) g_c can be found and it should be possible to the accurately describe the superradiant phase transition in the Holstein Primakoff approximation (of course a different HP-Hamiltonian has to be found for the superradiant phase, see next section). In case of $\epsilon > 0$, however, no real g_c exists and the subradiant phase transition is not reproduced. Whereas, in case of finite temperatures, fluctuations of observables have

to be considered in order to identify a phase transitions, the fact that ω_- and hence g_c do not change in the HP-model implies that rising temperature will not change the coupling strength at which the phase transition occurs.

4.4 Superradiant phase

We have seen that for coupling strengths $g > g_c$ the oscillator frequency ω_- becomes imaginary and hence Hamiltonian (4.39) no longer accurately describes the system at hand. The main features of the superradiant phase in the extended Dicke model are non-zero expectation values of the photonic creation and annihilation operators $\langle a \rangle = \sqrt{\alpha}$ aswell as of the spin operator S_x. In the Holstein-Primakoff approximation this means that also $\langle b \rangle = \sqrt{\beta} \neq 0$, $\langle b^\dagger b \rangle = \beta$ and hence $\sqrt{1 - \frac{b^\dagger b}{2S}}$ can no longer be approximated as 1. To circumvent this problem we introduce displaced operators c and d via $a \to c + \sqrt{\alpha}$ and $b \to d - \sqrt{\beta}$. Written in terms of the new operators we can then expand the square root in powers of S (where $k = 2S - \beta \sim \mathcal{O}(S)$ and assuming that $\alpha, \beta \sim \mathcal{O}(S)$, $g \sim \mathcal{O}(\frac{1}{\sqrt{S}})$, see [7])

$$x := \frac{\sqrt{2S}}{2}\sqrt{1 - \frac{b^\dagger b}{2S}} = \frac{\sqrt{k}}{2}\sqrt{1 - \frac{d^\dagger d - \sqrt{\beta}(d + d^\dagger)}{k}} \tag{4.45}$$

$$\approx \frac{\sqrt{k}}{2}\left(1 + \frac{\sqrt{\beta}}{2k}(d + d^\dagger) - \frac{d^\dagger d}{2k} - \frac{\beta}{8k^2}(d + d^\dagger)^2\right) + \mathcal{O}(\frac{1}{S}), \tag{4.46}$$

where we have introduced the new quantity x for convenience. Inserting this relation into S_x we can also write S_x and S_x^2 in terms of powers of $\sqrt{S}$ as

$$S_x = \frac{S_+ + S_-}{2} \approx d^\dagger x + x d - 2\sqrt{\beta} x = \tag{4.47}$$

$$= -\sqrt{\beta k} + \left(\frac{\sqrt{k}}{2} - \frac{\beta}{2\sqrt{k}}\right)(d + d^\dagger) + \left(\frac{1}{4}\sqrt{\frac{\beta}{k}} + \frac{1}{8}\left(\frac{\beta}{k}\right)^{\frac{3}{2}}\right)(d + d^\dagger)^2 \tag{4.48}$$

$$+ \frac{1}{2}\sqrt{\frac{\beta}{k}} d^\dagger d - \frac{1}{4}\sqrt{\frac{\beta}{k}} + \mathcal{O}(\frac{1}{\sqrt{S}}) \tag{4.49}$$

$$S_x^2 = \beta k + \left(\beta^{\frac{3}{2}} - \sqrt{\beta} k\right)(d + d^\dagger) + \left(\frac{k}{4} - \beta\right)(d + d^\dagger)^2 - \beta d^\dagger d + \frac{\beta}{2} + \mathcal{O}(\sqrt{S}). \tag{4.50}$$

S_z can be expressed in terms of the new bosonic operators c and d in a straightforward way, since the problematic square root is not present, as

$$S_z = \omega_{qb} b^\dagger b = \omega_{qb} \left(d^\dagger d - \sqrt{\beta}(d^\dagger + d) + \beta \right). \tag{4.51}$$

Inserting all these relations into H_{EDM} and neglecting terms of $\mathcal{O}(\frac{1}{\sqrt{S}})$ or smaller leads to

$$\begin{aligned} H_{HP}^{SR} = {} & \omega_c c^\dagger c + \left(\omega_0 + g\sqrt{\frac{\alpha\beta}{k}} - \frac{g^2}{\omega_c}(1+\epsilon)\beta \right) d^\dagger d + (\sqrt{\alpha}\omega_c - g\sqrt{\beta k})(c + c^\dagger) \\ & + g\left(\frac{\sqrt{k}}{2} - \frac{\beta}{2\sqrt{k}} \right)(c + c^\dagger)(d + d^\dagger) \\ & + \left(-\omega_0\sqrt{\beta} + g\sqrt{\alpha k} - g\beta\sqrt{\frac{\alpha}{k}} - \frac{g^2}{\omega_c}(1+\epsilon)\left(\sqrt{\beta}k - \beta^{\frac{3}{2}} \right) \right)(d + d^\dagger) \\ & + \left(\frac{g\sqrt{\alpha}}{4}\left(\frac{\beta}{k} \right)^{3/2} + \frac{g}{2}\sqrt{\frac{\alpha\beta}{k}} + \frac{g^2}{\omega_c}(1+\epsilon)\left(\frac{k}{4} - \beta \right) \right)(d + d^\dagger)^2 \\ & + \alpha\omega + \omega_0(\beta - S) - \frac{g}{2}\sqrt{\frac{\alpha\beta}{k}} - 2g\sqrt{\alpha\beta k} + \frac{g^2}{\omega}(1+\epsilon)\left(\beta k + \frac{\beta}{2} \right), \end{aligned} \tag{4.52}$$

which now contains the unknown quantities α and β as well as terms linear in bosonic operators. Demanding that the Hamiltonian should be bilinear, i.e. requiring that linear terms vanish, yields two equations which we can use to determine α and β:

$$\sqrt{\alpha} = \frac{gS}{\omega_c}\sqrt{1 - \left(\frac{\omega_c\omega_0}{2S\epsilon g^2} \right)^2} = \frac{g}{\omega}\sqrt{\beta k}, \tag{4.53}$$

$$\sqrt{\beta} = \sqrt{S\left(1 + \frac{\omega_c\omega_0}{2S\epsilon g^2} \right)}. \tag{4.54}$$

It is useful to introduce the new parameter

$$\mu = -\frac{\omega_c\omega_0}{2S\epsilon g^2} = -\frac{\omega_c\omega_0}{4\epsilon g'^2}, \tag{4.55}$$

where $g' = \frac{2g}{\sqrt{2S}}$; α, β and k (and in succession the Hamiltonian H_{HP}^{SR}) can then be written more compactly as

$$\sqrt{\alpha} = g'\sqrt{\frac{S}{2}(1-\mu^2)}, \tag{4.56}$$

$$\sqrt{\beta} = \sqrt{S(1-\mu)}, \tag{4.57}$$

$$\sqrt{k} = \sqrt{S(1+\mu)}. \tag{4.58}$$

Finally, plugging in the above relations, the Holstein-Primakoff Hamiltonian in the superradiant phase can be written as

$$\begin{aligned} H_{HP}^{SR} =& \omega_c c^\dagger c + \frac{\omega_0}{2\mu}(1+\mu)d^\dagger d + g'\mu\sqrt{\frac{2}{1+\mu}}(c+c^\dagger)(d+d^\dagger) \\ &+ \left(\frac{\omega_0(1-\mu)(1+3\mu)}{8\mu(1+\mu)} + f_\epsilon\right)(d+d^\dagger)^2 + C, \end{aligned} \tag{4.59}$$

where

$$C = -S\left(\frac{2g'^2}{\omega} + \omega_0\mu(1+\frac{1}{2\epsilon})\right) - \frac{g'^2}{\omega}(1-\mu) + \frac{g'^2}{\omega}(1+\epsilon)\left(2S(1-\mu^2)+1-\mu\right) \tag{4.60}$$

and $f_\epsilon = -\frac{\omega_0(1+\epsilon)}{2\epsilon}\frac{\mu}{1+\mu}$. A short comparison with (4.28) yields the remaining correspondences: $\omega_0 \leftrightarrow \omega_c$, $\omega_1 \leftrightarrow \frac{\omega_0}{2\mu}(1+\mu)$ and $\kappa \leftrightarrow \frac{\omega_0(1-\mu)(1+3\mu)}{8\mu(1+\mu)}$. Like before, the fully diagonalized Hamiltonian then reads

$$H_{HP} = \epsilon_+ e_+^\dagger e_+ + \epsilon_- e_-^\dagger e_- + \frac{1}{2}\left(\epsilon_+ + \epsilon_- - \omega - \omega_1\right) + C, \tag{4.61}$$

with polariton frequencies

$$\epsilon_\pm^2 = \frac{1}{2}\left(\omega_c^2 + \frac{\omega_{qb}^2}{\mu^2} - \frac{\omega_{qb}^2(1+\epsilon)}{\epsilon} \pm \sqrt{\left(\omega_c^2 - \frac{\omega_{qb}^2}{\mu^2} + \frac{\omega_{qb}^2(1+\epsilon)}{\epsilon}\right)^2 - \frac{4\omega_c^2\omega_{qb}^2}{\epsilon}}\right). \tag{4.62}$$

This Hamiltonian also exhibits a ground state-instability for $g = g_c$, this time, however ϵ_- is real for coupling strengths larger than g_c and becomes imaginary for $g < g_c$. Hence we have found the corresponding Holstein-Primakoff Hamiltonian for the extended Dicke model in the superradiant phase. Now it remains to be seen how well the approximate

HP-Hamiltonians reproduce the characteristics of the full EDM. We are going to do this in the next sections by comparing spectra as well as expectation values.

4.5 Expectation value of the electromagnetic energy

First, we have to derive the corresponding HP-expressions for the expectation values of the operators of interest. We will focus our efforts on the electromagnetic energy of the system, which is the part of the total energy given rise to by the cavity - the energy contained in cavity-excitations as well as interactions between cavity and dipoles. The operator can be read off H_{EDM} and is given by

$$H_{EM} = \omega_c a^\dagger a + g(a^\dagger + a)S_x + \frac{g^2}{\omega_c}S_x^2 \tag{4.63}$$

$$= \omega_c \left(a^\dagger + \frac{g}{\omega_c}S_x\right)\left(a + \frac{g}{\omega_c}S_x\right). \tag{4.64}$$

By inserting the relations for S_x and S_x^2 derived in the preceding sections we can find the corresponding HP-operator in terms of a, $a^\dagger$ and b, $b^\dagger$ or c, $c^\dagger$ and d, $d^\dagger$ in the normal phase or the superradiant phase respectively. These operators can, in turn, be replaced by the operators c_+, $c_+^\dagger$, c_-, $c_-^\dagger$ and e_+, $e_+^\dagger$, e_-, $e_-^\dagger$ of the corresponding polariton modes. Next, we normal order the resulting expressions. Thermal expectation values can then be calculated by taking the trace in the Fock base and since we are dealing with a bilinear, normal ordered expression only constants and terms proportional to the number operators will yield a non-zero contribution. To facilitate this straightforward, yet tedious calculation we resort to the use of the SNEG-package for MATHEMATICA (see [32]) which allows for analytic second-quantization calculations.

4.5.1 Normal phase

Following the described procedure we derive both ground state and thermal expectation value of the electromagnetic energy in the normal phase

$$\begin{aligned}\langle H_{EM}(0)\rangle = &-\frac{\omega_c}{2} + \frac{1}{4}(\omega_- \cos^2\gamma + \omega_+ \sin^2\gamma) + \frac{1}{4\omega_+}\left(2g'\cos(\gamma) + \omega_c \sin\gamma\right)^2 \\ &+ \frac{1}{4\omega_-}\left(2g'\sin\gamma - \omega_c\cos\gamma\right)^2,\end{aligned} \tag{4.65}$$

$$\langle H_{EM}(T)\rangle = \langle H_{EM}(0)\rangle + \frac{c_{N_+}}{e^{\beta\omega_+}-1} + \frac{c_{N_-}}{e^{\beta\omega_-}-1}, \tag{4.66}$$

$$c_{N_+} = \frac{\omega_+ \sin^2\gamma}{2} + \frac{1}{2\omega_+}\left(2g'\cos\gamma + \omega_c \sin\gamma\right)^2, \tag{4.67}$$

$$c_{N_-} = \frac{\omega_- \cos^2\gamma}{2} + \frac{1}{2\omega_-}\left(2g'\sin\gamma - \omega_c \cos\gamma\right)^2. \tag{4.68}$$

4.5.2 Superradiant phase

Equally, in the superradiant phase:

$$\langle H_{EM}(0)\rangle = \left[\frac{\epsilon_-}{4} + \frac{\omega_c^2}{4\epsilon_-} + \frac{g^2\omega_1}{4\epsilon_+\omega_c}\left(\frac{\beta^2}{k} - 2\beta + k\right)\right]\cos^2\gamma_2 + \left[\epsilon_- \Leftrightarrow \epsilon_+\right]\sin^2\gamma_2 \tag{4.69}$$
$$+ \frac{g\sqrt{\omega_c\omega_1}}{4}\left(\frac{1}{\epsilon_+} - \frac{1}{\epsilon_-}\right)\left(\sqrt{k} - \frac{\beta}{\sqrt{k}}\right)\sin(2\gamma_2),$$

$$\langle H_{EM}(T)\rangle = \langle H_{EM}(0)\rangle + \frac{c_{N_+}}{e^{\beta\epsilon_+}-1} + \frac{c_{N_-}}{e^{\beta\epsilon_-}-1}, \tag{4.70}$$

$$c_{N_+} = \frac{g^2\omega_1}{\epsilon_+\omega_c}\left[\frac{\beta^2}{2k} - \beta + \frac{k}{2}\right]\cos^2(\gamma_2) + \frac{g\sqrt{\omega_c\omega_1}}{2\epsilon_+}\left[\sqrt{k} - \frac{\beta}{\sqrt{k}}\right]\sin(2\gamma_2) \tag{4.71}$$
$$+ \left[\frac{\epsilon_+}{2} + \frac{\omega_c^2}{2\epsilon_+}\right]\sin^2\gamma_2,$$

$$c_{N_-} = \Big[\epsilon_- \Leftrightarrow \epsilon_+, \qquad \cos(\gamma_2) \Rightarrow \sin(\gamma_2), \qquad \sin(\gamma_2) \Rightarrow -\cos(\gamma_2)\Big]. \tag{4.72}$$

4.5.3 Transition point

Having derived the analytic formulas for the electromagnetic energy in both the normal and the superradiant phase, we notice that they comprise terms involving divisions by ω_- or ϵ_- respectively. Because these energies go to zero at the critical coupling strength g_c the questions as to the convergence of these terms arise; we will now show that they do, in fact, converge. To this end we write $g' = g'_c - \delta$ and caculate the limit $\delta \to 0$ of the terms

in question. In the normal phase we find

$$\lim_{\delta\to 0}\omega_- = 2\sqrt{\omega}\frac{|\epsilon|^{\frac{3}{4}}}{1+|\epsilon|}\sqrt{\delta}+\mathcal{O}(\delta), \tag{4.73}$$

$$\lim_{\delta\to 0}\left(g'\sin\gamma-\frac{\omega_c\cos\gamma}{2}\right)^2 = \frac{4|\epsilon|^3}{(1+|\epsilon|)^3}\delta^2+\mathcal{O}(\delta^3), \tag{4.74}$$

$$\lim_{\delta\to 0}(e^{\beta\omega_-}-1) = \beta\lim_{\delta\to 0}\omega_- = 2\beta\sqrt{\omega}\frac{|\epsilon|^{\frac{3}{4}}}{1+|\epsilon|}\sqrt{\delta}+\mathcal{O}(\delta), \tag{4.75}$$

$$\lim_{\delta\to 0}\frac{\omega_-}{e^{\beta\omega_-}-1} = \frac{1}{\beta}, \tag{4.76}$$

$$\lim_{\delta\to 0}\frac{\left(g'\sin\gamma-\frac{\omega_c\cos\gamma}{2}\right)^2}{\omega_-(e^{\beta\omega_-}-1)} = 0. \tag{4.77}$$

Hence, there are no divergences and the electromagnetic energy stays finite at $g = g_c$. Note, that in case of $\epsilon = -1$ equations (4.73) and (4.74) are exact for arbitrary δ. Of course, starting in the superradiant phase, defining $g' = g'_c + \delta$ and taking the limit $\delta \to 0$ must deliver the same results; we have checked numerically that the limits in both phases are consistent.

4.6 Comparison HP - full EDM

Having derived analytic results for the extended Dicke model in the Holstein Primakoff approximation, we are now going to investigate how the approximation holds up to the full model for various numbers of qubits and for different values of ϵ. The results for the full model have been acquired by means of a numerical simulation. Given the nature of the approximation, we expect agreement to be good for a large number of qubits and only rather crude for few qubits. In the following, we will compare the results for 4, 20 and 100 qubits.

4.6.1 $\epsilon = 0.5$

We have already found that for $\epsilon \geq 0$ HP does not predict a phase transition so we expect the approximation to fail for larger values of g, after the crossover to the subradiant phase has taken place in the full model. In figure 4.1 we compare the HP-spectrum to the full spectrum in case of 4 and 20 qubits. The results are as expected: for low coupling strengths the system is still in the normal phase and the approximation works well, especially in case of

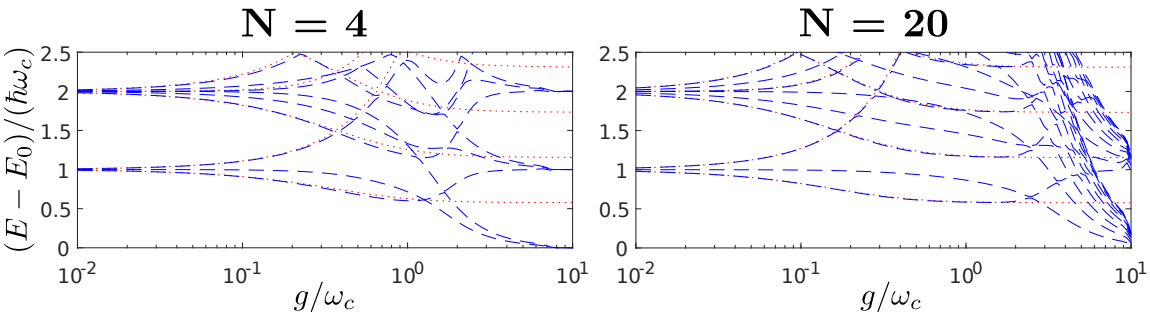

Figure 4.1: *Comparison of the spectra of the full EDM (blue dashed) and the HP approximation (red dotted) for 4 and 20 qubits at $\epsilon = 0.5$. At low coupling strengths the spectrum is nicely approximated even in case of just 4 qubits, although deviations become visible earlier than in the 20 qubit case. For 20 qubits agreement is very good up to $g \approx 1$, where discrepancies between the two models suddenly arise; for large coupling strengths HP does not reproduce the correct spectrum at all. These differences are due to the subradiant phase, which is not reproduced by the Holstein-Primakoff approximation.*

many qubits. At coupling strengths of $g \approx 1$, however, agreement abruptly stops, indicating the onset of the subradiant phase in the full model.

In addition to the spectrum we compare the ground state expectation values of the number operator $a^\dagger a$ and the electromagnetic energy H_{EM} in figure 4.2. For values $g < 1$ it is clearly visible that a higher number of qubits (20 instead of 4, in case of this figure) leads to a better approximation. In case of 20 qubits the approximation works well up to $g \approx 1$ where the subradiant phase transition takes place. In the full model, both photon number and electromagnetic energy return again to their initial values; in the Holstein-Primakoff approximation, however, the photon number remains near its maximum and the electromagnetic energy keeps rising indefinitely.

4.6.2 $\epsilon = -0.5$

For values of $\epsilon < 0$ HP predicts a phase transition, insofar we would expect the approximation to work well for both small and large coupling strengths g; in this section we are going to compare results for $\epsilon = -0.5$.

Fig. 4.3 depicts the spectrum of the HP spectrum together with the exact EDM spectrum. For small and large coupling strengths the approximation works well, independent of the number of qubits; in the intermediate regime, however, where the phase transition takes place, increasing the number of qubits clearly leads to much better results. There

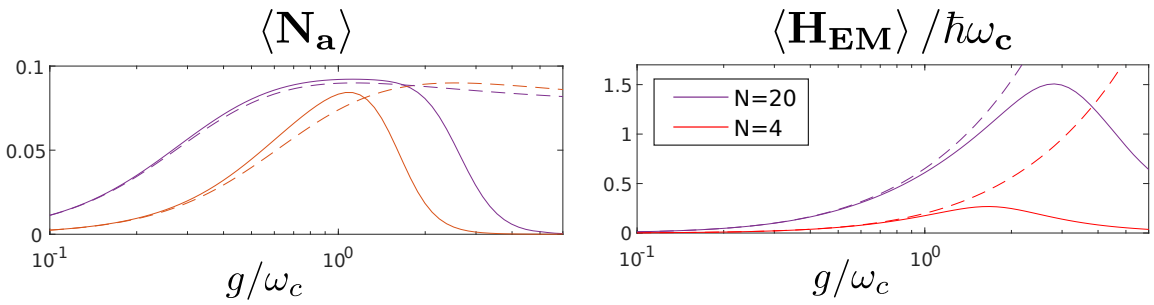

Figure 4.2: *Comparison of the ground state expectation values $\langle a^\dagger a \rangle$ and $\langle H_{EM} \rangle$ in the full model (full) and the HP approximation (dashed) for 4 and 20 qubits at $\epsilon = 0.5$. In the full model both expectation values show similar behaviour - an inital ascent followed by a subsequent descent back to their initial values, where the peak of the number operator-expectation value signifies the onset of the subradiant phase transition. In the HP model the expectation values are reasonably well reproduced for $g < 1$, especially in case of more qubits; as soon as the phase transition takes place in the full model, however, the predictions are in strong disagreement with the full model, as the electromagnetic energy keeps rising and the photon number does not descend rapidly.*

are lines in the EDM spectrum to which no equivalent exists in the HP spectrum; this is because in the Holstein-Primakoff approximation we only take the maximal spin-multiplet into account, whereas in the EDM, in order to get results that are as accurate as possible, we have included the contributions of all multiplets.

Next, we examine the results for the electromagnetic energy. In Fig. 4.4 the results for temperaturs $k_B T/\hbar\omega_c = 0, 0.5$ and 1 are shown. The outcome is unsurprising: in case of just 4 qubits deviations are visible not just in the area of the phase transition but throughout the ultrastrong coupling regime. In case of 20 qubits the approximation already delivers very reasonable results, only close to the peak of the curve, where the phase transition takes place, the two models deliver visibly distinct results. Finally, for 100 qubits, the Holstein Primakoff approximation is barely distinguishable from the exact model; only at higher temperatures a slight deviation around the peak becomes visible. The general trend, irrespective of qubit-number, as we go from low to high temperatures seems to be that disagreements between the models become more pronounced but the qualitative picture doesn't change.

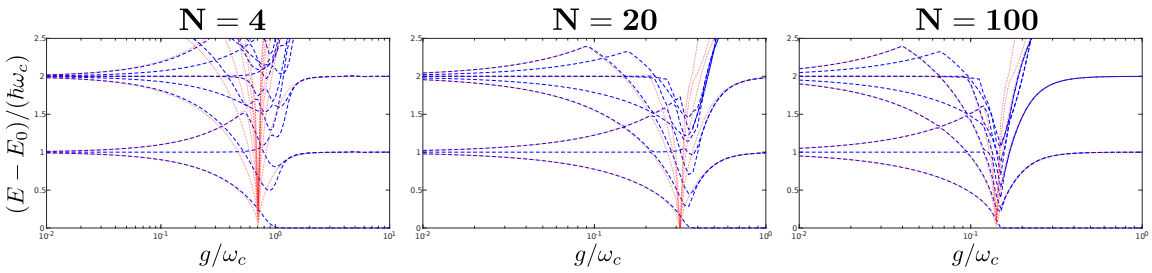

Figure 4.3: *Comparison of the Holstein-Primakoff spectrum (red dotted) to the exact spectrum of the extended Dicke model (blue dashed) at $\epsilon = -0.5$ for various numbers of qubits. In the limit of small or large coupling overall agreement is very good. In the area of the phase transition, however, it becomes apparent that the approximation works better for a higher number of qubits. Energy levels from the exact spectrum which are missing in the HP-spectrum belong to spin multiplets with $S < \frac{Nqb}{2}$; in the HP-approximation only the maximal spin-multiplet is taken into account.*

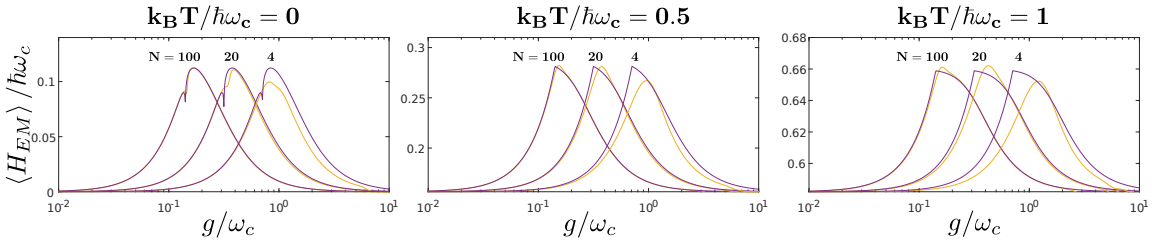

Figure 4.4: *Expectation value of H_{EM} in the Holstein-Primakoff approximation (purple) compared to the expectation value in the full extended Dicke model (yellow) for various numbers of qubits N_{qb} and temperatures $k_B T$ at $\epsilon = -0.5$. We see that for 4 qubits Holstein Primakoff, unsurprisingly, is only a very rough approximation. For 20 qubits deviations are only visible near the superradiant phase transition whereas for 100 qubits there is almost no difference. Going from temperature 0 to 1, we observe that agreement decreases with rising temperature but is still very good in case of a large number of qubits.*

4.7 Holstein-Primakoff - Summary

The Holstein-Primakoff approximation can be used to linearize the spin-part of the extended Dicke model and transform the EDM-Hamiltonian to an exactly solvable bilinear bosonic Hamiltonian. The diagonalization procedure and the calculation of expectation values is straightforward and can be facilitated by use of computer algebra environments like e.g. Mathematica together with the SNEG-package. Hence, a main advantage of using HP lies in the fact that in this model analytic expressions can be derived eliminating the need for possibly resource-intensive simulations.

The approximation is valid in case of $\epsilon < 0$ and a large number of qubits ($N_{qb} \gtrsim 20$). The spectrum as well as expectation values are reproduced very accurately from small coupling strengths across the superradiant phase transition. For a smaller number of qubits predictions are only very rough and for $\epsilon > 0$ the linearized model fails to capture the crossover to a subradiant phase and can therefore only be applied in case of small coupling strengths, where the system is still in the normal phase. The success of the Holstein-Primakoff approximation, in its respective range of validity, is due to the fact that the maximal spin multiplet constitutes the main contribution to observables like the electromagnetic energy.

Chapter 5

The EDM in the mean field approximation

5.1 The mean field approximation

An alternate method of deriving approximate results for the EDM can be found in mean field theory. In this approach interactions between different subsystems are not taken into account exactly, instead each component moves in an effective field caused by the other components. More formally, we demand that fluctuations of different subsystems be independent of each other:

$$((a+a^\dagger)-\langle a+a^\dagger\rangle)(\sigma_x^i-\langle\sigma_x^i\rangle)=0, \tag{5.1}$$

$$(\sigma_x^i-\langle\sigma_x^i\rangle)(\sigma_x^j-\langle\sigma_x^j\rangle)=0. \tag{5.2}$$

These relations can be manipulated to give expressions for the interaction terms $(a+a^\dagger)\sigma_x^i$ and $\sigma_x^i\sigma_x^j$ which depend on operators of only one subsystem. Inserting them into the DM (where only the first relation is of importance) or EDM Hamiltonian yields

$$H_{DM}^{MF}=\omega_c a^\dagger a+\sum_i\left[\frac{\omega_{qb}}{2}\sigma_z^i+\frac{g}{2}(\langle a+a^\dagger\rangle\,\sigma_x^i+\langle\sigma_x^i\rangle\,(a+a^\dagger)-\langle a+a^\dagger\rangle\,\langle\sigma_x^i\rangle)\right], \tag{5.3}$$

in case of the Dicke model or

$$H_{EDM}^{MF} = H_{DM}^{MF} + \frac{g^2}{\omega_c}(1+\epsilon)\frac{N\langle\sigma\rangle}{2}\sum_i \sigma_x^i - \frac{g^2N^2\langle\sigma\rangle^2(1+\epsilon)}{4\omega_c}, \tag{5.4}$$

in case of the extended Dicke model. These Hamiltonians are now of the form $H = H_{qb}+H_c$ which means that the partition function $Z = Tr(e^{-\beta H})$ factorizes into two parts which can be calculated analytically. After abbreviating the expectation values via $\alpha = \langle a\rangle = \langle a^\dagger\rangle$ (where the last equality is equivalent to requiring α to be real), $S_x = \frac{1}{2}\sum_i \langle\sigma_x^i\rangle$ we obtain

$$Z_{DM} = \left(2\cosh\left(\beta\sqrt{\left(\frac{\omega_{qb}}{2}\right)^2 + (g\alpha)^2}\right)\right)^N \frac{e^{\beta(\frac{(gS_x)^2}{4\omega_c}+g\alpha S_x)}}{1-e^{-\beta\omega_c}} \tag{5.5}$$

and

$$\begin{aligned} Z_{EDM} =& \exp\left(\beta\left(\frac{(gS_x)^2}{4\omega_c} + \alpha g S_x + \frac{g^2S_x^2(1+\epsilon)}{4\omega_c}\right)\right) \\ &\times \frac{\left(2\cosh\left(\beta\sqrt{\left(\frac{\omega_{qb}}{2}\right)^2 + \left(g\alpha + \frac{g^2}{\omega_c}\frac{(1+\epsilon)}{2}S_x\right)^2}\right)\right)^N}{1-e^{-\beta\omega_c}}. \end{aligned} \tag{5.6}$$

Given Z, the free energy

$$F = -k_BTlnZ \tag{5.7}$$

can be calculated and using the fact that in thermal equilibrium α and S_x must take on values such that F is minimal. Therefore we can find equations to determine these parameters via

$$\frac{\partial F}{\partial \alpha} = 0, \tag{5.8}$$

$$\frac{\partial F}{\partial S_x} = 0. \tag{5.9}$$

Inserting F yields the two equations

$$\frac{\partial F}{\partial \alpha} = -N\tanh(\xi)\frac{\beta}{\xi}\left(g\alpha + \frac{g^2(1+\epsilon)S_x}{2\omega_c}\right)g - gS_x = 0, \tag{5.10}$$

$$\frac{\partial F}{\partial S_x} = -N\tanh(\xi)\frac{\beta}{\xi}\left(g\alpha + \frac{g^2(1+\epsilon)S_x}{2\omega_c}\right)\frac{g^2(1+\epsilon)}{2\omega_c} - g\alpha \tag{5.11}$$

$$-\frac{g^2S_x(1+\epsilon)}{2\omega_c} - \frac{g^2S_x}{2\omega_c} = 0, \tag{5.12}$$

with

$$\xi = \beta\sqrt{\frac{\omega_{qb}^2}{4} + \left(g\alpha + \frac{g^2(1+\epsilon)S_x}{2\omega_c}\right)^2}. \tag{5.13}$$

This leads to the relation between S_x and α

$$S_x = \frac{2\alpha\omega_c\omega_{qb}}{g}\kappa, \tag{5.14}$$

where $\kappa = ((1+\epsilon)(\omega_c - \omega_{qb}) - \omega_{qb}))^{-1}$ and subsequently, by inserting S_x into one of the initial equations, to an equation for α:

$$-N\tanh(\xi)\left(1 + \omega_c\kappa(1+\epsilon)\right)\alpha g^2 = 2\omega_c\omega_{qb}\alpha\kappa\beta\xi. \tag{5.15}$$

$\alpha = 0$ is the obvious solution and corresponds to the normal phase. If we require that $\alpha \neq 0$ we can divide by α and obtain a transcendental equation for α which has to be solved numerically. We can, however, find an analytic result for the critical coupling strength g_c at which α is exactly zero. In case of $T = 0$ the hyperbolic tangent becomes 1 and we find

$$g_c(0) = \sqrt{\frac{\omega_c\omega_{qb}}{N}}\sqrt{\frac{-\omega_{qb}\kappa}{1 + (1+\epsilon)\omega_c\kappa}} = \sqrt{\frac{\omega_c\omega_{qb}}{N}}\sqrt{\frac{-\omega_{qb}}{2\omega_c(1+\epsilon) - (2+\epsilon)\omega_{qb}}} \tag{5.16}$$

wich reduces to

$$g_c(0) = \sqrt{\frac{-\omega_c^2}{N\epsilon}} \tag{5.17}$$

in case of $\omega_c = \omega_{qb}$. For finite temperatures we get the equation

$$\frac{g_c(T)}{g_c(0)} = \tanh\left(\frac{\hbar\omega_{qb}}{2k_BT}\right)^{-\frac{1}{2}}. \tag{5.18}$$

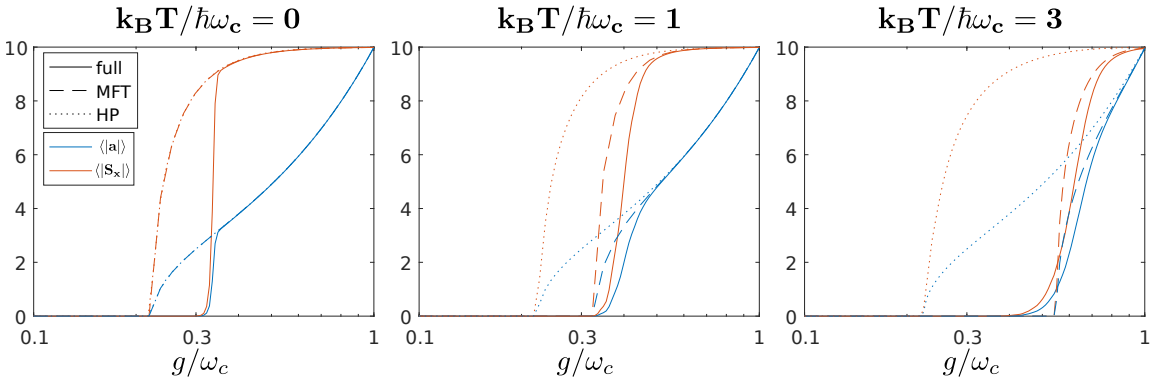

Figure 5.1: *Comparison of the expectation values of the operators a and S_x in the full model, in the Holstein-Primakoff approximation and in mean field theory. At zero temperature HP and MFT predict the same results. As we go to higher temperatures, the predictions of HP don't change much whereas the results of MFT seemingly become more accurate.* $N_{qb} = 10$, $\epsilon = -1$

Hence, the mean field approach predicts a temperature-dependent critical coupling strength. Vice versa, at a given $g/g_c(0)$, we can find the critical temperature T_c at which the superradiant phase vanishes by inverting relation (5.18).

5.2 Results and limitations

In figure 5.1 we compare predictions for the expectation values of the operators a and S_x in all three models: the full model, the HP approximation and in mean field theory. At temperature zero both HP and MFT predict the same results but as we go to higher temperatures the results of HP don't change significantly whereas MFT seemingly becomes more accurate. This is most likely due to the fact that with rising temperature quantum fluctuations are suppressed and the underlying assumption of mean field theory is more justified.

It is important, however, to keep in mind the limitations of the mean field approach; since we have assumed that fluctuations of the subsystems of the EDM are independet of each other expectation values of the electromagnetic energy or the U^2-term cannot be reproduced accurately. In the end, the mean field approach is suitable to estimate the temperature-dependent critical coupling strength $g_c(T)$ (see figure 3.1) of the SRT and to calculate expectation values that do not depend on quantum fluctuations.

Chapter 6

Heat capacity of cavity QED systems

In this section we will investigate the thermal behaviour of the extended Dicke model by calculating the heat capacity of the system. In particular, we are interested to find out how the coupling between cavity mode and atoms alters the heat capacity when compared to the uncoupled systems. Starting out with the extended Dicke model Hamiltonian (where cavity and qubits are in resonance)

$$H_{\mathrm{EDM}} = \omega a^\dagger a + \omega S_z + g(a^\dagger + a)S_x + \frac{g^2}{\omega}(1+\epsilon)S_x^2, \tag{6.1}$$

we introduce two modifications: firstly, we add a parameter v which allows us to tune the coupling between cavity and dipoles, without affecting the dipole-dipole term, secondly we express the dipole-dipole interaction term differently in terms of the inter-dipole coupling strength $J = \frac{g^2}{\omega}\epsilon$. This highlights the fact that the pure inter-dipole coupling is independent of the cavity-dipole coupling; only the ϵ is changed by it. Now we can write our Hamiltonian as

$$H = \omega a^\dagger a + \omega S_z + g\sqrt{v}(a^\dagger + a)S_x + \frac{g^2}{\omega}vS_x^2 + JS_x^2. \tag{6.2}$$

Setting $v = 0$ turns off the coupling between cavity and atoms and leads to the Lipkin-Meshkov-Glick (LMG) model [33]; note, that here we use a version of the LMG model that contains both the spins and the cavity mode. In case of $v = 1$ the coupling is present and we recover the EDM.

According to HP, the EDM ($v = 1$) undergoes the transition to the superradiant phase

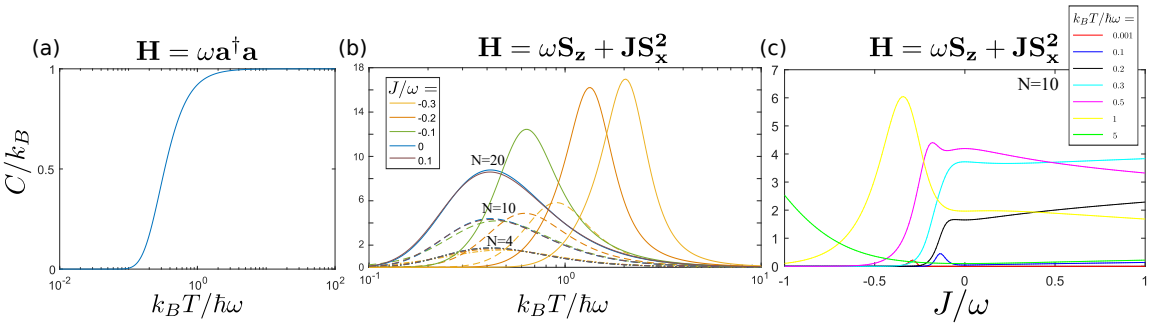

Figure 6.1: *(a) Heat capacity of a harmonic oscillator. (b) Heat capacity of* $N = 4, 10$ *and* 20 *spins for different values of* J*. For values of* $J < J_c$ *position and shape of the curve are very sensitive to* J*, whereas in case of* $J > J_c$ *the curve remains almost unchanged. An explanation for this behaviour can be found in the low-energy part of the spectrum: if it is dominated by the* JS_x^2*-term, the dependency of the heat capacity on* J *will be large. (c) Heat capacity of a 10 qubit system as a function of the inter-qubit coupling* J *at different temperatures. The phase transition taking place at* $J \approx J_c$ *is clearly discernible.*

at an inter-dipole coupling strength of

$$J_c = -\omega/N, \tag{6.3}$$

which translates again into the critical coupling strength derived before in section 4.1,

$$g_c = \sqrt{\frac{-\omega^2}{N\epsilon}}. \tag{6.4}$$

6.1 Heat capacity of uncoupled systems

First, in order to be able to better interpret the subsequent results, we are going to set $v = 0$ to take a look at the heat capacity of the uncoupled constituents of the whole system, i.e. the bare oscillator and the spins. Adding both together leads to the heat capacity of the LMG model, which according to our definition includes the decoupled cavity mode.

In figure 6.1 we have depicted the heat capacity of the harmonic oscillator as well as that of the spin system for different values of the total spin and different values of inter-spin coupling. The heat capacity of the harmonic oscillator is, of course, the same as usual: it starts rising at temperatures $k_BT \approx \hbar\omega/10$ and at $k_BT = \hbar\omega$ it has almost reached its maximum value of $C/k_B = 1$.

The spin case is more interesting, since different values of J can result in qualitatively different eigentstates; for $J < J_c$ alignment of the spins (in the ground state) in x-direction is energetically favorable, whereas otherwise the z-direction is preferred. In our plots we are going to consider a variety of values for the inter-spin coupling strength, both above and below this threshold.

As can be seen from figure 6.1 (b), where C/k_B is depicted for 4, 10 and 20 qubits, the heat capacity of the pure spin system is very sensitive to the inter-spin coupling strength in case of $J < J_c$; both the temperature at which it starts to rise as well as the location of it's maximum and the maximum value itself are clearly distinguishable. In case of $J > J_c$, however, it barely changes. This can be attributed to the fact that the heat capacity is most sensitive to the exact distribution of the energy levels at low temperatures; at higher temperatures slight alterations are averaged over. In case of $J < J_c$ the low energy behavior of the system is dominated by the JS_x^2-term, hence the sensitivity of the heat capacity with respect to J. For values of $J > J_c$, on the other hand, the ωS_z-term constitutes the major contribution to the heat capacity and changing J does not have much of an effect.

Figure 6.1 (c) depicts the heat capacity as a function of J at various temperatures in case of 10 qubits. The aforementioned phase transition taking place at $J \approx J_c$ is clearly discernible.

6.2 Heat capacity of composite system

Having taken a look at the seperate systems in the previous section, we are now going to investigate the influence of coupling between cavity and spins on the heat capacity of the composite system. As we have seen previously, the extended Dicke model undergoes a phase transition/a crossover as the coupling strength enters the ultrastrong coupling regime; accordingly, we expect the heat capacity to undergo significant changes as well.

In the subsequent figures we are going to plot both the heat capacity of the EDM and the contribution of the cavity-dipole coupling to it. We calculate the latter by subtracting the heat capacity of the LMG model from that of the EDM, that is

$$C_{\text{int}} := C_{\text{EDM}} - C_{\text{LMG}}. \tag{6.5}$$

In figure 6.2 the heat capacity is plotted against the coupling strength g. Comparing both the full heat capacity of the EDM as well as the contribution due to the coupling, it

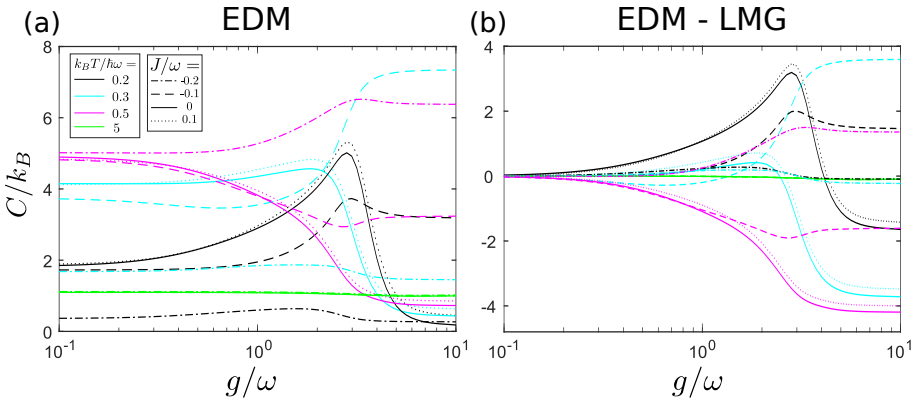

Figure 6.2: $N_{qb} = 10$*: Heat capacity of (a) the extended Dicke model and (b) the contribution effected by the cavity-dipole coupling as a function of g for different values of J and at various temperatures. The overall contribution of the coupling to* C_{EDM} *keeps rising up to intermediate temperatures but eventually goes to zero again for temperatures above the cavity frequency; at such temperatures variations in the spectrum are no longer resolved by the heat capacity. Since the LMG model does not depend on g, all changes of the heat capacity in this plot originate in the cavity-dipole coupling.*

becomes apparent that all observable changes are due to the coupling term; this makes sense, since the LMG model does not depend on the coupling strength. With rising temperature, overall contributions to C_{EDM} due to the coupling increase at first, up to intermediate temperatures of $k_BT \approx 0.5\hbar\omega$. Subsequently, C_{int} decreases again and at $k_BT = 5\hbar\omega$ it is practically zero. This last observation can be understood as follows: at high temperatures, many states are in reach of thermal excitations and contribute to the specific heat; the ups and downs of the various energies in the eigenspectrum are therefore averaged over and their overall contribution no longer changes notably with g.

Figure 6.3 shows the heat capacity as a function of the inter-qubit coupling strength J at various temperatures and for different values of g. For low enough temperatures, an abrupt change, due to the transition from the superradiant to the subradiant phase, is observable for values of J/ω near $J_c/\omega = 0.1$. The bulk of these changes is contained in the contribution of the interaction part of the heat capacity; after all, it is the coupling between cavity and qubits that gives rise to the different phases.

Finally, in figure 6.4, we compare the magnitude of the contribution of the cavity-dipole coupling to the overall heat capacity for various numbers of qubits at small and large coupling strengths. Additionally, we have plotted the heat capacity of the pure spin system,

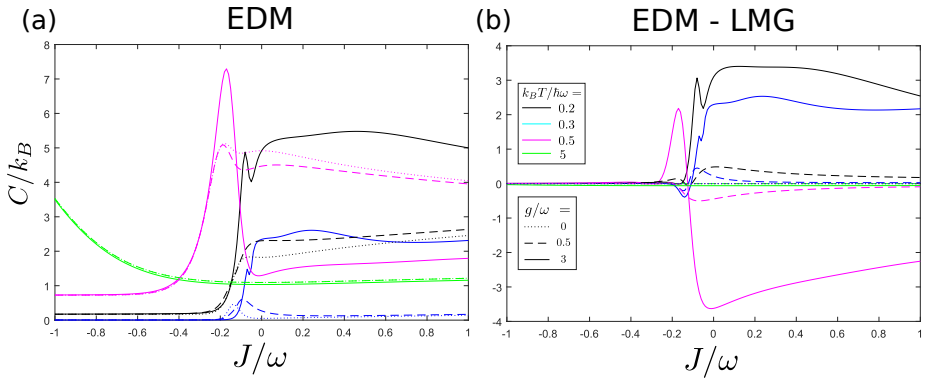

Figure 6.3: $N_{qb} = 10$*: Heat capacity of (a) the extended Dicke model and (b) the contribution effected by the cavity-dipole coupling as a function of* J *for different values of* g *and at various temperatures. Rapid changes that are visible at* $J/\omega \approx -0.1$ *hint at the transition between sub- and superradiant phase.*

to be able to better compare the relative strength of the contributions. Unsurprisingly, for a given number of qubits and for increasing coupling strengths, C_{int} increases as well. From the plot with $g/\omega = 5$ we see that, in case of $J = 0$, C_{int} can reach and even surpass in magnitude the heat capacity of the pure spin system; most notably, C_{int} apparently scales with the number of qubits. This observation can be traced back to the 2^N-fold (nearly) degenerate manifolds in the spectrum of the EDM for $J = 0$ (or, in this case, equivalently $\epsilon = 0$).

6.3 Heat capacity - summary

We have investigated the contribution C_{int} to the heat capacity C_{EDM} of the entire EDM due to the cavity-dipole coupling. As is to be expected from the significant qualitative changes which the eigenspectrum of the EDM undergoes with rising coupling strength, C_{int} can constitute a major contribution to the overall heat capacity and reflects transitions between the different phases. In case of $J = 0$ and for large coupling strengths g, C_{int} reaches values similar or even larger in magnitude than the heat capacity of the pure spin system and scales with the number of qubits.

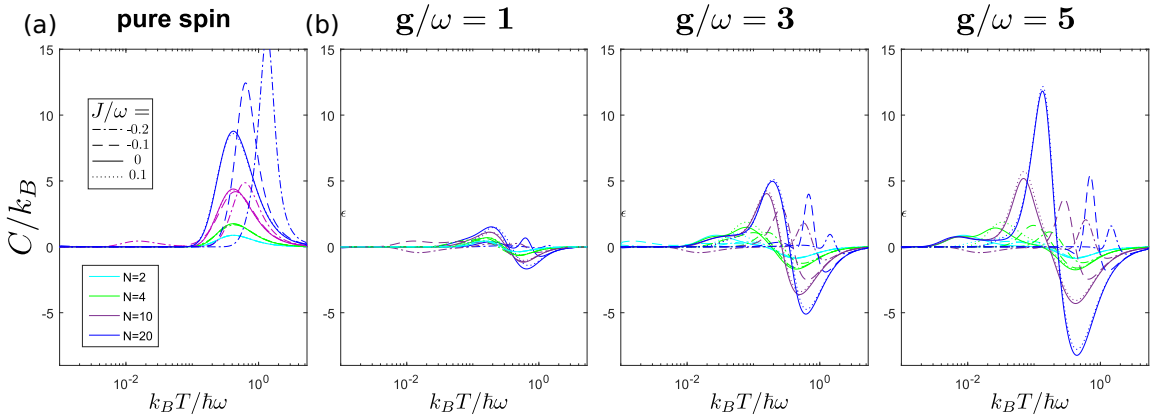

Figure 6.4: *(a) Heat capacity of the uncoupled spin system and (b) contribution of cavity-spin coupling to C_{EDM} as a function of temperature, for different values of g and J and multiple numbers of qubits. At high coupling strengths and for $J = 0$, C_{int} can reach and even surpass the magnitude of the heat capacity of the pure spin system and scales visibly with the number of qubits.*

Part III

Numerics

Chapter 7

Numerics

In this part we are going to give a brief overview of the techniques employed to obtain the numerical results discussed throughout the work. This includes both analytic transformations of the Hamiltonian which allow for resource-intensive calculations to be split up into many parts as well as some heuristic measures that were taken to estimate the convergence of the results.

7.1 Block-diagonal structure of the EDM-Hamiltonian

In earlier parts of the work we have introduced the extended Dicke model in the form

$$H_{\mathrm{EDM}} = \omega_c a^\dagger a + \omega_0 S_z + g(a^\dagger + a)S_x + \frac{g^2}{\omega_c}(1+\epsilon)S_x^2, \tag{7.1}$$

where the $S_i = \frac{1}{2}\sum_i \sigma_i$ are total spin matrices which contain the contribution of each individual spin. Using the relation $[S^2, S_j] = 0$ it can readily be shown that the EDM-Hamiltonian commutes with the square of the total spin operator S^2, $[H_{\mathrm{EDM}}, S^2] = 0$. This means that H_{EDM} can be brought into block-diagonal form, with each block corresponding to one eigenvalue of the total spin operator, i.e. the different spin-multiplets that can be formed by the individual spins.

Considering each possible spin-multiplet individually greatly reduces the resources that are required in our calculations. Initially, dealing with non-collective spins, there are 2^N spin-states to be taken into account simultaneously; switching to the collective picture and treating each subspace separately breaks this number down to $2S+1$ states, where S is

the collective spin of the multiplet. For the biggest possible subspace with $S = \frac{N}{2}$, we have $N+1$ states, a tremendous improvement compared to 2^N for large N. Naturally, the total number of states has to remain unchanged but summing over the states provided by each S-subspace only results in $\sum_S 2S+1 = \frac{N}{2}(\frac{N}{2}+1) + \frac{N}{2} + 1 = (\frac{N}{2}+1)^2$ states; this discrepancy can be resolved by taking into account the multiplicity of the different spin multiplets.

7.2 Multiplicity of spin multiplets

In order to be able to calculate expectation values for temperatures above absolute zero we must know the degeneracy of each state and hence the multiplicity of the various spin multiplets that can be formed out of N coupled spin-1/2 systems. This can be achieved by considering the Clebsch-Gordan fusion rule (or, more generally, the Clebsch-Gordan decomposition, see e.g. [34]), which describes the coupling of a doublet to an N-multiplet, a multiplet with N possible orientations:

$$\underline{2} \otimes \underline{N} = \underline{N+1} \oplus \underline{N-1}. \tag{7.2}$$

Mathematically speaking, we find the direct sum decomposition of the tensor product space in which the two multiplets live. Formula (7.2) can be understood as follows: take a spin-S and couple to it a spin-1/2; the spin-1/2 can either align itself or anti-align itself to the spin-S, thereby increasing or decreasing the total spin by 1/2. A spin-S corresponds to a $(2S+1)$-multiplet, hence the formula. Starting with one spin-1/2 and repeatedly coupling additional ones to it we can find the multiplicity for ever higher numbers of spins by using the Clebsch Gordan fusion rule:

$$N = 1: \quad \underline{2} \tag{7.3}$$

$$N = 2: \quad \underline{2} \otimes \underline{2} = \underline{3} \oplus \underline{1} \tag{7.4}$$

$$N = 3: \quad \underline{2} \otimes \underline{2} \otimes \underline{2} = \underline{2} \otimes (\underline{3} \oplus \underline{1}) = \underline{4} \oplus \underline{2} \oplus \underline{2} = \underline{4} \oplus 2\underline{2} \tag{7.5}$$

$$N = 4: \quad 2^{\otimes 4} = \cdots = \underline{5} \oplus 3\underline{3} \oplus 2\underline{1} \tag{7.6}$$

$$\vdots \tag{7.7}$$

Using this scheme a general formula on how N spins can be arranged into multiplets can be derived:

$$2^{\otimes N} = \bigoplus_{k=0}^{\lfloor \frac{N}{2} \rfloor} m_{N,k} \underline{N+1-2k}, \tag{7.8}$$

with

$$m_{N,k} = \frac{N!(N+1-2k)}{k!(N+1-k)!}. \tag{7.9}$$

Using $k = \frac{N-2S}{2}$, we can also write the multiplicity directly in terms of S as

$$m_{N,S} = \frac{N!(2S+1)}{(\frac{N}{2}-S)!(\frac{N}{2}+S+1)!}. \tag{7.10}$$

This result is in agreement with other methods of obtaining the multiplet-multiplicity.

7.3 The EDM in the polaron frame

One problem, when it comes to numerical simulations of the EDM as given in (7.1), even after taking into account the block-diagonal structure, is the high number of photon states that has to be taken into account in order to get accurate results at high coupling strengths and temperatures. In the superradiant phase this number quickly reaches the hundreds. This number does not correspond to the actual number of cavity photons but arises due to the fact that in the dipole picture this number corresponds to excitations of the electric displacement field. One way to circumvent this problem is to switch to the polaron frame where the photon number again corresponds to the actual number of photons, which remains much smaller, via $H' = UHU^\dagger$ where $U = e^{\frac{g}{\omega_c} S_x (a^\dagger - a)}$ [1, 35]. This can also be thought of as transforming back to the Coulomb picture after having made the 2-state approximation in the dipole picture.

We can make use of Hadamard's Lemma,

$$e^A B e^{-A} = B + [A,B] + \frac{1}{2!}[A,[A,B]] + \frac{1}{3!}[A,[A,[A,B]]] + \dots \tag{7.11}$$

$$= e^{ad(A)} B, \tag{7.12}$$

to calculate how the relevent operators change under the polaron transformation:

$$UaU^\dagger = a + \frac{g}{\omega_c} S_x, \tag{7.13}$$

$$Ua^\dagger U^\dagger = a^\dagger + \frac{g}{\omega_c} S_x, \tag{7.14}$$

$$US_zU^\dagger = \frac{1}{2}\left[e^{\frac{g}{\omega_c}(a^\dagger - a)}(S_z - iS_y) + e^{-\frac{g}{\omega_c}(a^\dagger - a)}(S_z + iS_y)\right]. \tag{7.15}$$

The transformed Hamiltonian is then given by

$$H'_{\mathrm{EDM}} = UH_{\mathrm{EDM}}U^\dagger = \omega_c a^\dagger a + \frac{g^2}{\omega_c}(1+\epsilon)S_x^2 + \frac{\omega_0}{2}\left(e^{-\frac{g}{\omega_c}(a^\dagger - a)}\tilde{S}_- + e^{\frac{g}{\omega_c}(a^\dagger - a)}\tilde{S}_+\right), \tag{7.16}$$

where the exponentials just correspond to the displacement operator $D(\alpha) = e^{\alpha(a^\dagger - a)}$ and $\tilde{S}_\pm = S_z \pm iS_y$ are the ladder operators with respect to S_x. A formula for the matrix elements of $D(\alpha)$ in the Fock basis is given in [36],

$$\langle m|\, D(\xi)\, |n\rangle = \left(\frac{n!}{m!}\right)^{\frac{1}{2}} \xi^{m-n} e^{-\frac{|\xi|^2}{2}} L_n^{m-n}(|\xi|^2), \tag{7.17}$$

where the L_n^{m-n} denote associated Laguerre polynomials.

7.4 Number of states to consider in simulations

Since the system at hand is described by an infinite-dimensional Hilbert-space it is impossible to include all states. Firstly, this issue arises when deciding how many Fock-states to include when calculating the eigenstates of the system. Secondly, we must determine states up to what energy have to be included to yield accurate thermal expectation values.

7.4.1 Determine the maximum photon-number N_a

In order to determine the number of Fock states, $N_a + 1$, to include in our calculations, it has proven useful to think of the maximum photon number in terms of the maximum energy $E_{\max}$; states with energies up to $E_{\max}$ are included when calculating thermal expectation values. Arguing, simply, that the higher the energy of the system the more photons it can

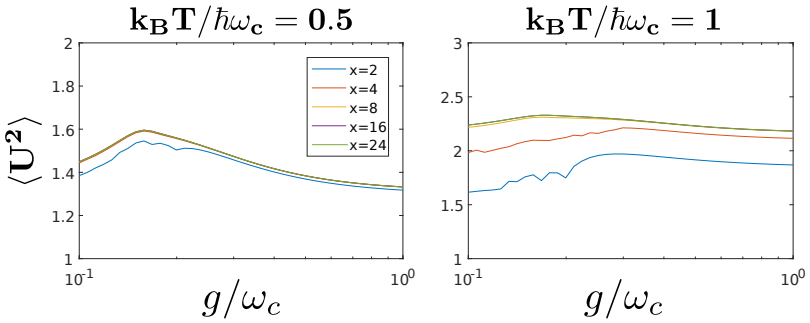

Figure 7.1: *Comparison of the values received for the expectation value $\langle U^2 \rangle$ when taking into account states up to higher and higher energies, i.e. for various ratios $x = (E_{\max} - E_0)/k_B T$. It is apparent that in case of a temperature of $k_B T/\hbar\omega_c = 0.5$ a value of $x = 4$ is sufficient, whereas for $k_B T/\hbar\omega_c = 1$ a choice of $x = 16$ seems to be ideal. ($N = 50$, $\epsilon = -1$)*

contain, suggests making the ansatz

$$N_a = a \left\lceil \frac{E_{\max} - E_0}{\hbar\omega_c} \right\rceil, \qquad a \in \mathbb{N}, \tag{7.18}$$

for our photon number, where the rounding brackets, $\lceil\ \rceil$, are required to ensure an integer result.

Empirically, we find that $a = 1$ works very well in case of $\epsilon < 0$, whereas for values $\epsilon > 0$ a value of $a = 8$ is required to go up to $g/\omega_c \approx 10$.

7.4.2 Determine the maximum energy $E_{\max}$

Next, we would like to get an estimate on how many states must be taken into account in order to get reliable thermal expectation values for finite temperatures. We introduce the new parameter x and define the cut-off energy as a multiple of the thermal energy via $E_{\max} - E_0 := x k_B T$; eigenstates with energy $\epsilon_k \leq E_{\max}$ are taken into account. In Fig. 7.1 we have plotted the expectation value $\langle U^2 \rangle$ for various values of x. As can be seen from the graph, one has to go up to at least $x = 8$, or ideally $x = 16$ for temperatures up to $k_B T \lesssim \hbar\omega_c$. The higher the temperature, the higher x has to be and when calculating expectation values up to $k_B T/\hbar\omega_c = 10$ we have chosen $x = 20$.

The U^2-operator has been chosen as reference since, with U being given by $U = \frac{1}{\sqrt{2}}(a + a^\dagger + \frac{2g}{\omega_c} S_x)$, it comprises most of the operators of interest.

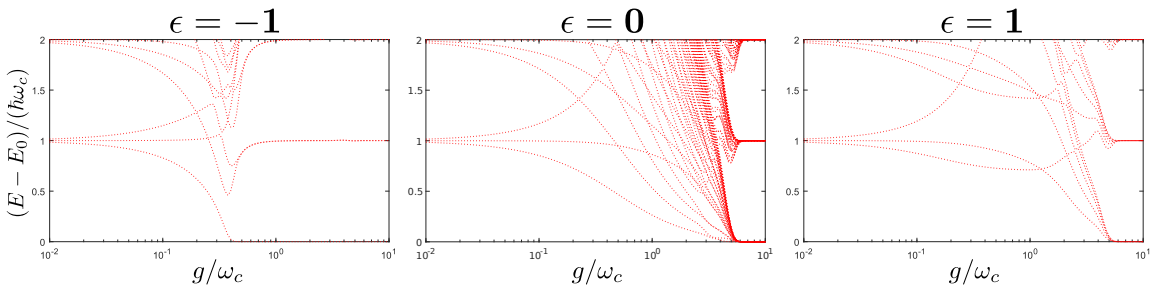

Figure 7.2: *Plot of the spectrum of the extended Dicke model for different values of ϵ. ($N = 4$)*

Having determined heuristically a cutoff energy, we now would like to take a look at the energy spectrum of the EDM to find out the relationship between the value of x and the number of states to take into account. Fig. (7.2) shows the characteristics of the spectrum for $\epsilon = -1, 0, 1$. As can be seen from the figure, different values of ϵ can lead to qualitatively different spectra. In the weak coupling regime, where $g \approx 0$, the spectrum is still independent of ϵ and we observe nearly degenerate subspaces. Here, where the coupling is still small, the degeneracy is given by the number of ways in which excitations of the cavity mode and the spin system can be combined to result in the energy at hand.

For a given spin-multiplet, the degeneracy is one in case of the ground state. The degeneracy then increases by one for each subsequent manifold, e.g. in case of the first excited manifold we can either have one photon and a multiplet orientation resulting in the magnetic quantum number $m_S = -S$ or no photon and $m_S = -S + 1$, whereas in case of the second excited manifold three possibilities exist: zero photons and $m_S = -S + 2$, one photon and $m_S = -S + 1$ and two photons together with $m_S = -S$. This scheme can be continued up to the energy at which all possible multiplet orientations, together with a suitable number of photons, can result in a state of the given energy. In other words, at $g = 0$, states with energy $(E - E_0)/\hbar\omega_c = 2S$ and above will have a degeneracy of $2S + 1$.

7.4.3 Number of states up to $E_{\max}$

In case of $\epsilon = 0$ and in the limit $g \gg \omega$ the spectrum consists of 2^N-fold (nearly) degenerate manifolds (see [1]). Each such manifold contains states of different spin manifolds as $2^N = \sum_S m_{N,S}(2S+1)$. Hence, for a given spin multiplet S we have to calculate $n_S = \lfloor x k_B T/\hbar\omega_c + 1 \rfloor (2S+1)$ states. This number can quickly become quite large, e.g. for $x = 16$, $k_B T/\hbar\omega_c = 1$

we find $n_{50} = 1717$. Hence, for $\epsilon \approx 0$ a compromise of some sort will be required, be it a smaller factor x or a lower temperature.

For $\epsilon > 0$ and large g, each manifold of nearly degenerate states contains $\sum_S m_{N,S}$ states; each multiplet contributes one state.

Hence, for low and large coupling strengths and arbitrary ϵ we can count the number of states below a certain energy. Knowing these limits also allows us to estimate for the coupling strengths in-between; when in doubt, a number of state that suffices in case of $\epsilon = 0$ and large g will also be enough elsewhere. When calculating spectra, it is most convenient to start with the result for low coupling strengths and then dynamically adjust the number of states. At each step we calculate a few states more than required and check if the maximal energy is still above or below a certain threshold; if not, the number of states will be increased or reduced accordingly.

Conclusions and outlook

In part I of my thesis we revisited the derivation of effective cavity-QED models and demonstrated the importance of making the correct choice of gauge when performing the two-level approximation. Controversies surrouding the quantum Rabi model in form of a 'no-go theorem' and a 'counter no-go theorem' have been resolved. The electric dipole gauge has been shown to be clearly superior to the Coulomb gauge when truncating the Hilbert space to derive the QRM in the single-dipole case or the (extended) Dicke model in the multi-dipole case. We have used a superconducting circuit to demonstrate our findings using the example of a realistic setup. Overall, it has been shown that the two-state model in the electric dipole gauge and in case of sufficiently nonlinear atoms delivers accurate results up to coupling strengths well within the ultrastrong coupling regime.

In part II, the thermodynamics of the extended Dicke model have been investigated. I examined the effect of non-zero temperatures on the superradiant phase transition and on the crossover to the subradiant phase; with increasing temperature, both the phase transition and the crossover are smeared out over a larger interval of coupling strengths. Once the thermal energy $k_B T$ surpasses the energy of the bare cavity mode $\hbar\omega_c$, changes in observables due to the transitions can no longer be discerned from the background noise due to thermal fluctuations, which are now present in the system.

Two different approximations have been employed to enable the derivation of analytic results for the extended Dicke model. Firstly, the spin-part of the EDM has been bosonized via the Holstein-Primakoff approximation. For a number of qubits larger than 20 this approximation describes the SRT very well and deviations from the full model are only visible nearby the phase transition; both eigenspectrum and expectation values can be calculated. Secondly, I applied mean field theory to the EDM by neglecting correlations between the fluctuations of different constituents of the system. While this approach cannot be used to calculate the eigenspectrum it predicts the onset of the superradiant phase

transition more accurately than HP. Neither of the two approximations reproduces the crossover to the subradiant phase for $\epsilon > 0$.

Furthermore, the heat capacity of the extended Dicke model as well as that of its constituents has been calculated; in particular, I investigated the influence of the cavity-dipole coupling on this quantity. The maximum value of the heat capacity of the pure spin system depends on the number of individual spins; an analogous scaling with the number of qubits has been observed for the contribution to the heat capacity by the coupling term in case of $\epsilon = 0$.

In part III I elaborated on mathematical methods and properties of the EDM that can be used to simplify numerical simulations. Firstly, considering different spin-multiplets separately greatly reduces the size of the Hilbert space at hand. Secondly, switching to the polaron frame reduces the required number of Fock states to be included in the simulations. Furthermore, the heuristics were detailed, which I used to estimate proper cutoff energies as well as suitable numbers of states to take into account.

One possible avenue of future research would be to use the extended Dicke model to calculate the quantum capacity of an LC-resonator, where atoms have been placed between the plates of the capacitor. Results obtained here could then be compared to a classical model where the atoms are treated collectively as a dielectric material filling the capacitor.

It would also be interesting to compile a phase diagram of the EDM depending on J instead of ϵ; since J is the more natural quantity to consider, such a diagram could facilitate an intuitive understanding of the different phases of the extended Dicke model.

Bibliography

[1] T. Jaako, Z.-L. Xiang, J.J. Garcia-Ripoll, and P. Rabl, Ultrastrong coupling phenomena beyond the Dicke model, Phys. Rev. A **94**, 033850 (2016).

[2] G. Chen, X. Wang, J. -Q. Liang, and Z. D. Wang, Exotic quantum phase transitions in a Bose-Einstein condensate coupled to an optical cavity, Phys. Rev. A **78**, 023634 (2008).

[3] R. H. Dicke, Coherence in Spontaneous Radiation Processes, Phys. Rev. **93**, 99 (1954).

[4] B. M. Garraway, The Dicke model in quantum optics: Dicke model revisited, Phil. Trans. R. Soc. **369**, 1137 (2011).

[5] K. Hepp, and E. H. Lieb, On the superradiant phase transition for molecules in a quantized radiation field: the dicke maser model, Ann. Phys. **76**, 360 (1973).

[6] Y. K. Wang, and F. T. Hioe, Phase Transition in the Dicke Model of Superradiance, Phys. Rev. A **7**, 831 (1973).

[7] C. Emary, and T. Brandes, Chaos and the Quantum Phase Transition in the Dicke Model, Phys. Rev. E **67**, 066203 (2003).

[8] D. De Bernardis, T. Jaako, and P. Rabl, Cavity quantum electrodynamics in the nonperturbative regime, Phys. Rev. A **97**, 043820 (2018).

[9] R. J. Thompson, G. Rempe, and H. J. Kimble, Observation of normal-mode splitting for an atom in an optical cavity, Phys. Rev. Lett. **98**, 1132 (1992).

[10] T. G. Tiecke, J. D. Thompson, N. P. de Leon, L. R. Liu, V. Vuletić, and M. D. Lukin, Nanophotonic quantum phase switch with a single atom, Nature **508**, 241 (2014).

[11] A. Wallraff, D. I. Schuster, A. Blais, L. Frunzio, R. S. Huang, J. Majer, S. Kumar, S. M. Girvin, and R. J. Schoelkopf, Strong coupling of a single photon to a superconducting qubit using circuit quantum electrodynamics, Nature (London) **431**, 162 (2004).

[12] A. Blais, R.-S. Huang, A. Wallraff, S. M. Girvin, and R. J. Schoelkopf, Cavity quantum electrodynamics for superconducting electrical circuits: an architecture for quantum computation, Phys. Rev. A **69**, 062320 (2004).

[13] J. Q. You, and F. Nori, Atomic physics and quantum optics using superconducting circuits, Nature (London) **474**, 589 (2011).

[14] X. Mi, J. V. Cady, D. M. Zajac, P. W. Deelman, and J. R. Petta, Strong Coupling of a Single Electron in Silicon to a Microwave Photon, Science **355**, 156 (2017).

[15] A. Stockklauser, P. Scarlino, J. V. Koski, S. Gasparinetti, C. K. Andersen, C. Reichl, W. Wegscheider, T. Ihn, K. Ensslin, and A. Wallraff, Strong Coupling Cavity QED with Gate-Defined Double Quantum Dots Enabled by a High Impedance Resonator, Phys. Rev. X **7**, 011030 (2017).

[16] C. Ciuti, G. Bastard, and I. Carusotto, Quantum vacuum properties of the intersubband cavity polariton field, Phys. Rev. B **72**, 115303 (2005).

[17] P. Forn-Diaz, L. Lamata, E. Rico, J. Kono, and E. Solano, Ultrastrong coupling regimes of light-matter interaction, arXiv:1804.09275 (2018).

[18] P. Nataf, and C. Ciuti, No-go theorem for superradiant quantum phase transitions in cavity QED and counter-example in circuit QED, Nature Commun. **1**, 72 (2010).

[19] A. Vukics, and P. Domokos, Adequacy of the Dicke model in cavity QED: a counter-"no-go" statement, Phys. Rev. A **86**, 053807 (2012).

[20] D. De Bernardis, P. Pilar, T. Jaako, S. de Liberato, and P. Rabl, Breakdown of gauge invariance in ultrastrong coupling cavity QED, Phys. Rev. A **98**, 053819, (2018).

[21] D. Braak, Q. Chen, M. T. Batchelor, and E. Solano, Semiclassical and quantum Rabi models: in celebration of 80 years, J. Phys. A: Math. Theor. **49**, 300301 (2016).

[22] S. Ashhab, Superradiance transition in a system with a single qubit and a single oscillator, Phys. Rev. A **87**, 013826 (2013).

[23] Y. Todorov, and C. Sirtori, Intersubband polaritons in the electrical dipole gauge, Phys. Rev. B **85**, 045304 (2012).

[24] O. Viehmann, J. von Delft, and F. Marquardt, Superradiant Phase Transitions and the Standard Description of Circuit QED, Phys. Rev. Lett. **107**, 113602 (2011).

[25] J. J. Hopfield, Theory of the Contribution of Excitons to the Complex Dielectric Constant of Crystals, Phys. Rev. **112**, 1555 (1958).

[26] V. E. Manucharyan, J. Koch, L. I. Glazman, and M. H. Devoret, Fluxonium: Single cooper-pair circuit free of charge offsets, Science **326**, 113 (2009).

[27] M. H. Devoret, Quantum Fluctuations in Electrical Circuits, Les Houches, Session LXIII, (1997).

[28] U. Vool, and M. Devoret, Introduction to Quantum Electromagnetic Circuits, arXiv:1610.03438 (2016).

[29] T. Holstein, and H. Primakoff, Field Dependence of the Intrinisic Domain Magnetization of a Ferromagnet, Phys. Rev. **58**, 1098 (1940).

[30] C. Tsallis, Diagonalization methods for the general bilinear Hamiltonian of an assembly of bosons, Journal of Mathematical Physics **19**, 277 (1978).

[31] O. Maldonado, On the Bogoliubov transformation for quadratic boson observables, Journal of Mathematical Physics **34**, 5016 (1993).

[32] R. Zitko, SNEG - Mathematica package for symbolic calculations with second-quantization-operator expressions, Comp. Phys. Comm. **182**, 2259 (2011).

[33] H. J. Lipkin, N. Meshkov, and A. J. Glick, Validity of many-body approximation methods for a solvable model: (I). Exact solutions and perturbation theory, Nucl. Phys. **62**, 188 (1965).

[34] A. Zee, Group Theory in a Nutshell for Physicists, Princeton University Press, ISBN 978-0691162690 (2016).

[35] Q.-H. Chen, Y.-Y. Zhang, T. Liu, and K.-L. Wang, Numerically exact solution to the finite-size Dicke model, Phys. Rev. A **78**, 051801(R) (2008).

[36] K. E. Cahill, and R. J. Glauber, Ordered Expansions in Boson Amplitude Operators, Phys. Rev. **177**, 5 (1969).